



DIPLOMARBEIT

Lokalisierungsstudien für Gamma-Ray Bursts mit dem Satelliten SPHiNX

zur Erlangung des akademischen Grades

DIPLOM-INGENIEUR/IN

im Rahmen des Studiums

TECHNISCHE PHYSIK

eingereicht von

LEA ALINA HECKMANN

Matrikelnummer 1226232

ausgeführt am ATOMINSTITUT

der Fakultät für Physik

der TECHNISCHEN UNIVERSITÄT WIEN

in Zusammenarbeit mit

Prof. MARK PEARCE und Dr. NIRMAL KUMAR IYER

von der KÖNIGLICHE TECHNISCHE HOCHSCHULE STOCKHOLM

unter der Anleitung von

Privatdoz. Dr.rer.nat. MANFRED JEITLER

SEPTEMBER 9,
2018

UNTERSCHRIFT STUDENTIN

UNTERSCHRIFT BETREUERIN



MASTERTHESIS

Gamma-ray Burst Localisation Studies for the SPHiNX Satellite

to obtain the academic degree

DIPLOM-INGENIEUR/IN

within the scope of the degree program

ENGINEERING PHYSICS

submitted by

LEA ALINA HECKMANN

Student ID 1226232

performed at the ATOMIC INSTITUTE

at the Faculty of Physics

at the VIENNA UNIVERSITY OF TECHNOLOGY

in cooperation with

Prof. MARK PEARCE and Dr. NIRMAL KUMAR IYER

KTH ROYAL INSTITUTE OF TECHNOLOGY STOCKHOLM

under supervision of

Privatdoz. Dr.rer.nat. MANFRED JEITLER

Abstract

The Satellite Polarimeter for High eNergy X-rays (SPHiNX) is a proposed satellite mission designed to measure the polarisation of the prompt emission phase of gamma-ray bursts (GRBs) within the range of 50-600 keV. GRBs are bright flashes in the sky originating from the mergers of compact objects or super-massive star collapses. Determining the polarisation angle and degree of the highly energetic radiation is predicted to improve the understanding of the radiative processes taking place at the emitting site. An essential parameter for the polarimetric performance is the knowledge of the GRB location since it is proven to influence the polarisation figures of merit. An uncertainty of 5° or less in the polar angle of the GRB with respect to the polarimeter is expected to be crucial for an unimpaired polarimeter performance.

The feasibility study investigating the localisation capability of SPhINX introduces three methods using Monte-Carlo simulations. The most basic approach exploits the geometric correlation between hit patterns inside the detector and the azimuthal GRB position, while the more advanced methods are based on producing databases of hit patterns and their comparison with test datasets by applying the statical methods of χ^2 minimisation and maximum likelihood. Four parameters were defined to validate the methods and localisation capability: viz. the offsets and uncertainties in the azimuthal (ϕ) and polar (θ) angles.

The geometric method has the advantage of giving fast azimuthal positioning without depending on the GRB energy spectrum. Both azimuthal offset and uncertainty show a sinusoidal dependency on the original azimuthal position. While the uncertainty stays inside 1.5 - 2.5° , the offset peaks at 10° . First estimations for the polar uncertainty predict an order of magnitude of around 5° . The two database methods show strong dependencies on the energy spectrum used to produce the database. This dependency is accounted for by rescaling databases to the relevant spectrum due to the assumption that the GRB spectrum can be reconstructed during operation using the response matrix of SPhINX. The obtained localisation results are mostly influenced by the original polar angle. For most positions within the field of view, the offsets and uncertainties stay inside the 5° limits, some higher values can occur for more central positions, however. While these results were obtained by using GRBs with median fluences, the localisation precision improves for higher intensities. SPhINX lacks the necessary sensitivity to measure polarisation for GRBs with weaker fluences.

In conclusion, sufficiently precise localisation results seem to be obtainable, which leads to a positive impression of the SPhINX localisation capability.

Kurzfassung

Das Satelliten-Polarimeter für hoch energetische Röntgenstrahlen (SPHiNX) ist eine vorgeschlagene Satellitenmission mit dem Ziel, die Polarisation der prompten Emission von Gammablitz (GRB) im Energiebereich von 50-600 keV zu messen. Gammablitz sind intensive, hoch energetische Explosionen, welche ein- bis zweimal am Tag zufällig am Himmel auftreten. Es wird angenommen, dass sie durch die Verschmelzung zweier kompakter Objekte oder des Kernkollapses eines super-massiven Sterns entstehen. Polarisationsmessungen könnten Aufschluss darüber geben, wie die Strahlungsemission der Gammastrahlen dabei vor sich geht. Die Positionsbestimmung der beobachteten Gammablitz ist ein wichtiger Parameter für die polarimetrische Leistung, da die Unschärfe der Positionsbestimmung Auswirkungen auf die Kennzahlen der Polarisationsmessung hat. Die Kenntnis der Position innerhalb eines 5° Rahmens, insbesondere der polaren Komponente, ist notwendig, um die Polarisationsmessungen nicht zu beeinträchtigen.

Diese Projektstudie untersucht die Lokalisierungsfähigkeit von SPHiNX mithilfe dreier Methoden basierend auf Monte-Carlo Simulationen. Die erste dieser Methoden stützt sich auf die geometrische Korrelation zwischen dem Hit-Muster innerhalb des Detektors und dem Azimutalwinkel des GRBs. Zur Durchführung der beiden anderen Vorgehensweisen werden Datenbanken von Hit-Mustern erzeugt und mit Test-Mustern durch die statistischen Methoden der χ^2 -Minimierung oder der Maximierung der Likelihood-Funktion verglichen. Dabei dienen vier Parameter als Validierung der Methoden und der Lokalisierungsfähigkeit von SPHiNX: viz. die Offsets und Unschärfen des azimutalen und polaren Winkels.

Die geometrische Methode hat den Vorteil einer sehr schnellen und einfachen Bestimmung des Azimutalwinkel ohne von dem Energiespektrum des Gammablitzes abhängig zu sein. Sowohl der Offset als auch die Unschärfe zeigen eine sinusförmige Abhängigkeit zum ursprünglichen Azimutalwinkel. Während die Unschärfe innerhalb von 1.5 - 2.5° fluktuiert, befinden sich die Spitzen der Offset-Sinuskurve bei 10° . Beide Datenbankmethoden dokumentieren eine starke Abhängigkeit von dem in der Datenbank verwendeten GRB Energiespektrum. Dies wird durch eine Skalierung der Datenbank zu dem gewünschten Spektrum ausgeglichen, wobei das benötigte GRB Spektrum während der Mission mithilfe der "response matrix" von SPHiNX rekonstruiert werden kann. Die erhaltenen Lokalisierungsergebnisse scheinen großteils vom ursprünglichen Polarwinkel beeinflusst zu sein. Für die meisten Positionen innerhalb des Sichtfeldes von SPHiNX befinden sich sowohl die Offsets wie auch die Unschärfen innerhalb der 5° . Etwas höhere Werte können für zentralere Positionen auftreten. Diese Resultate wurden mithilfe von mittel-intensiven Gammablitz ermittelt, wobei sich die Lokalisierungsgenauigkeit mit steigender Intensität weiter verbessert. SPHiNX ist nicht sensitiv genug, um die Polarisation von GRBs mit schwächeren Intensitäten zu messen.

Zusammenfassend ergibt diese Machbarkeitsstudie ausreichend gute Lokalisierungsergebnisse, die einen positiven Eindruck für die Lokalisierungsfähigkeit von SPHiNX erlauben.

Sammanfattning

SPHiNX är ett föreslaget satellitprojekt för att utföra polarisationsmätningar av gammablixtar (GRBs). Mätningarna kan hjälpa till att förstå processerna bakom strålningsemissionen. Lokaliseringen av gammablixtarna är en viktig parameter för polarimeterns prestanda, eftersom precisionen direkt påverkar polarisationsmätningarnas mätetal. Positionsnoggrannheten av polarvinkeln måste vara minst 5° för att inte polarimeterns polarisationsmätningar ska försämrats.

I en förstudie har SPhINX förmåga att lokalisera gammablixtar undersökts genom att studera tre Monte Carlo-baserade simuleringar. Den första metoden drar nytta av det geometriska sambandet mellan hit-mönstret i detektorn och gammablixtens azimutvinkel. I de två andra metoderna produceras databaser av hit-mönstren och jämförs med data genom att applicera de statistiska metoderna χ^2 minimisation och Maximum likelihood. Fyra parametrar har valts ut för att validera metoderna och SPhINX förmåga att lokalisera: viz. offseten och precision av polär och azimutal vinkeln.

Den geometriska metoden har till fördel att den ger ett snabbt och enkelt resultat för azimutvinkeln utan att vara beroende av gammablixtens energispektrum. Såväl differensen som precisionen påvisar ett sinusformat beroende av den reella azimutvinkeln, vilket medger offsetkorrektioner. Precisionen är mellan $1.5\text{--}2^\circ$ men differensen kan uppgå till 10° på maximumet av sinuskurvan. Båda databas-metoderna påvisar ett starkt beroende av de energispektra som används för att skapa databaserna. Detta beroende tas i beaktande genom att databaserna skalas till relevant spektra, vilket kan göras tack vare antagandet att gammablixtarnas spektra kan rekonstrueras med hjälp av SPhINX responsmatris. De erhållna resultaten verkar mestadels påverkas av den polära vinkeln. För de mest signifikanta regionerna stannar den polära vinkelns offset på under 5° . För centrala positioner kan högre värden förekomma. Dessa resultat har erhållits genom att studera gammablixtar med medium luminositet. För högre intensiteter förbättras precisionen ytterligare.

Sammanfattningsvis indikerar studien att tillräckligt precis lokalisering är möjlig, vilket leder till ett positivt intryck av SPhINX lokaliseringsförmåga.

Contents

1	Introduction	2
1.1	Author's Contribution	3
2	X-ray Polarimetry	4
2.1	Fundamental Principles	4
2.1.1	Photon Interactions in a Detector	4
2.1.2	Polarisation of electromagnetic Waves	7
2.2	Compton Polarimetry	7
2.3	Gamma-Ray Bursts as polarised Emission Sources	9
2.3.1	Gamma-Ray Bursts	9
2.3.2	Emission Processes	10
3	The SPHiNX Detector	13
3.1	SPHiNX Science Goal	14
3.1.1	Jet Structure	14
3.1.2	Jet Magnetisation	14
3.1.3	Emission Mechanism	15
3.2	Design	16
4	Localisation Methodology	19
4.1	Simulation Setup	20
4.1.1	Data Processing and single Hit Selection	23
4.2	Modulation Curve Method	25
4.3	χ^2 Minimisation Method	29
4.4	Maximum Likelihood Method	32
5	Results and Discussion	35
5.1	Modulation Curve Method	35
5.2	χ^2 Minimisation Method	39
5.3	Maximum Likelihood Method	43
5.4	Method Comparison	47
5.5	Estimations including Background	47
5.6	Total localisation uncertainty	50
5.7	Conclusions and Outlook	52
	References	58

Chapter 1

Introduction

“Remember to look up at the stars and not down at your feet. Try to make sense of what you see and wonder about what makes the universe exist. Be curious.”

- Stephen Hawking

Ironically, one of the brightest mysteries of our universe was discovered the exact opposite way. While searching for underground nuclear tests, the US Vela satellite happened to see a bright flash of gamma-rays randomly appearing in the sky. Now, more than 50 years later, it is known that these so-called gamma-ray bursts (GRBs) happen once or twice per day at different positions in the sky and could play an important role in understanding and probing our universe. [1] Nonetheless, there is still a large number of riddles connected with GRBs waiting to be solved. Even though the simultaneous observation of a gravitational wave together with a GRB and its optical afterglow in August 2017 [2] proved the connection between GRBs and the mergers of compact objects, the basic emission processes behind GRBs still give rise to many speculations. The principles of the underlying radiative processes as well as the magnetic and geometric structure of the emitted jets remain hidden, entangled in the complex physical systems involved.

One component so far mostly understudied in our age of multi-messenger astronomy could help to shed light on the undiscovered secrets. X-ray polarimetry has the possibility of measuring the polarisation parameters of the prompt, highly energetic emission of GRBs. By comparing these results to theoretical predictions, different models could be distinguished taking another step towards a deeper understanding of our universe.

The proposed Satellite Polarimeter for High eNergy X-rays (SPHiNX) has been designed to obtain these parameters. It is predicted to be capable of measuring the polarisation of around 50 GRBs during its planned operation time of two years, which would lead to a statistically significant contribution to the small amount of recent polarisation data.

One of the challenges during these measurements is the entanglement of information about the polarisation parameters, energy spectrum and location of the GRBs in the observed data. Therefore, knowledge of the GRB spectrum and location is vital for polarisation analysis. In the convenient case of other GRB detectors up in the sky designed to measure exact these properties, data from these missions are supposed to be used. However, since the launch time and therefore the distribution of other GRB detectors is yet unknown, an internal localisation method has to be developed.

In addition, information about GRB locations serves as valuable input for follow-up observations. Dedicated missions are designed to localise GRBs with very high precision.

However, these missions do not cover the whole sky and the future situation is yet to be planned. Hence, SPHiNX localisation could play an additional role of providing at least coarse initial GRB location for GRB alerts.

As a preliminary feasibility study, different localisation methods were developed and investigated, such as exploding geometric dependencies in the hit patterns or database comparisons via χ^2 minimisation or maximum likelihood methods proving the localisation capability of the SPHiNX polarimeter.

In the following chapters, the relevant theory and methods to perform the localisation studies for the SPHiNX polarimeter will be presented. A motivation for X-ray polarimetry together with its basic theory will be given in Chapter 2. It includes explanations of the physical processes involved as well as the fundamental principle of Compton polarimetry. In addition, the phenomena of gamma-ray bursts and theories explaining their emission processes are specified. Thereafter, the SPHiNX detector together with its components and scientific motivation will be introduced in Chapter 3. The methodology explaining the simulation and analysis methods used in the localisation studies will be defined in Chapter 4. In conclusion, the results for the localisation uncertainties for the different methods as well as the various systematic influences on the results will be presented in Chapter 5.

1.1 Author's Contribution

The aim of my thesis was to perform the preliminary localisation studies for the SPHiNX detector. This involved adapting the existing simulation set-up to the purpose needed and choosing suitable methods for the localisation studies. My role was to design these methods and carry out the simulations and analysis. The results can be found in Chapter 5 proving promising feedback for the localisation capability of SPHiNX.

During the whole project, results were presented at SPHiNX collaboration meetings and constant feedback was received.

Chapter 2

X-ray Polarimetry

In the current age of multi-messenger astronomy the secrets of our universe become more and more probable to be revealed. One of the channels which could help to answer some of the open questions is X-ray polarimetry. The polarisation of photons which are continuously observed from the vast number of objects in the sky could help to reveal different processes happening close to these complex objects.

One of the still not entirely understood phenomena are gamma-ray bursts. Even after decades of observations the main processes of how and in what form these highly energetic photons are emitted are unknown. X-ray polarimetry has the ability to determine the polarisation properties of these photons, which could help to shed light on the hidden processes happening at the emission sites.

This chapter will provide the underlying theories for understanding X-ray polarimetry. First, important physical effects will be explained, such as the different interaction of highly energetic photons with detectors or the basics of polarisation. Especially the theory of Compton polarimetry, which is the central principle behind the SPHiNX detector, will be presented in detail. Afterwards, the source of polarised emission relevant for SPHiNX, the so-called gamma-ray bursts, and their main emission models will be described together with the open questions connected to these phenomena.

2.1 Fundamental Principles

2.1.1 Photon Interactions in a Detector

Considering particle detectors, three main interaction between photons and matter can be stated, if the photon energies are higher than the ionisation energy of the material: The photoelectric effect, Compton scattering and pair production. Which of these processes is dominant depends on the photon energies as well as the atomic number of the interacting material as displayed in Figure 2.1. The likelihood of these events will be described by stating the characteristic cross section, an effective area, that defines the interaction probability.

In this section, the three main interaction processes will be introduced together with their cross sections and relevant energy regions. Besides, the optical process of scintillation will be explained as scintillators are the main component used in Compton polarimetry.

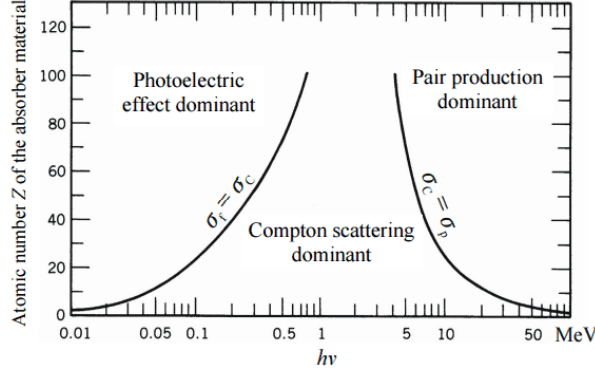


Figure 2.1: Dependency of the attenuation coefficient of different photon-matter interaction on the photon energy and the atomic number of the absorbing material [3].

Photoelectric Effect

For lower energies, the photoelectric effect is dominating. If a photon with higher energy than the ionisation energy of the material hits an atom, its total energy is absorbed and transferred to the emission of one of its electrons. Calculating the photoelectric cross section for all energies is known to be very complicated and mostly based on different approximations. For the most relevant energy region the Born cross section

$$\sigma_{\text{ph}}^{\text{NR}} \propto \frac{Z^n}{E^m} \quad (2.1)$$

with $n = 4 - 5$ and $m \leq 3.5$ is considered as a good approximation for non-relativistic energies. It is based on the Born approximations while taking the conservation of angular momentum into consideration. Variations of n and m with energy are dependent on the correction factor arising due to the transfer of angular momentum from the photon to the electron.

The cross section can be seen as $\sigma_{\text{p.e.}}$ in Figure 2.2. The edges in the curve can be explained due to the different shells of the atom with different ionisation energies. The probability of the photoelectric effect decreases with increasing photon energies.

If a photon deposits its total energy in the detector without electrons escaping the detector, the so-called "photo-peak" will be seen as a typical characteristic in the energy spectrum of the detector [4].

Compton Scattering

Compton scattering describes the scattering of a photon on a free or quasi-free electron, which is the case if the photon energy is far higher than the electron binding energy. It is dominant in the region around 1MeV, being wider for lower Z .

The energy and angle of the scattered photon and electron are linked to each other due to conservation laws as displayed in Figure 2.3. By using quantum electrodynamics the differential cross section, which defines the cross section for a given solid angle, for Compton scattering can be obtained and is known as Klein-Nishina-Formula [5]

$$\frac{d\sigma_{\text{C}}}{d\Omega} = \frac{1}{2} r_{\text{e}}^2 \epsilon^2 [\epsilon + \epsilon^{-1} - 2\sin^2\theta] \quad (2.2)$$

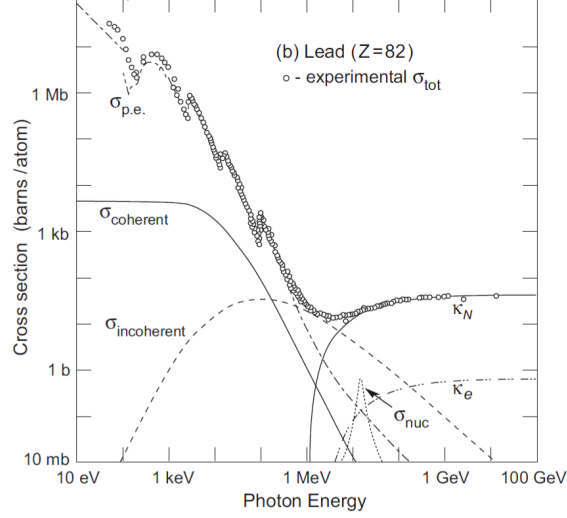


Figure 2.2: Cross section of the photon interaction with lead ($Z=82$). Displayed are the total cross section (σ_{tot}), the photoelectric effect ($\sigma_{\text{p.e.}}$), Compton scattering ($\sigma_{\text{incoherent}}$) and pair production at the nuclei (κ_N) as well as the coherent Rayleigh scattering (σ_{coherent}), the photoelectric effect at the nuclei (σ_{nuc}) and pair production at the electron shells (κ_e) [4].

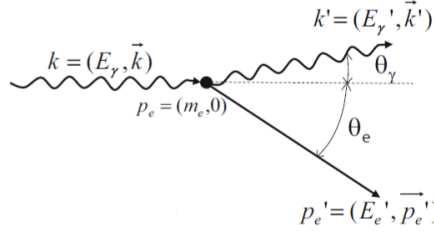


Figure 2.3: Kinematic of a Compton scattering process [4].

where

$$\epsilon = \frac{E'_\gamma}{E_\gamma} = \frac{1}{1 + (E_\gamma/m_e c^2)(1 - \cos\theta)} \quad (2.3)$$

with E_γ being the initial photon energy, E'_γ the photon energy after scattering, m_e the electron mass, c the speed of light, r_e the classical electron radius and θ the scattering angle of the photon. This cross section is displayed as $\sigma_{\text{incoherent}}$ in Figure 2.2.

The maximal energy transfer to the electron takes place when the photons are scattered in the backward direction, which corresponds to forward scattering of the electron. This can be seen as the so-called "Compton-edge" in the energy spectrum of the detector [4].

Pair Production

For high energies, pair production becomes the relevant interaction process. A photon in a Coulomb field can produce an electron-positron pair if its energy is higher than the two electron masses. This process is shown in Figure 2.4.

The cross section can be obtained by using quantum mechanics and the Born approximations, which leads to a Z^2 dependency and almost no dependency on the photon energy [4]. It is displayed as κ_N in Figure 2.2.

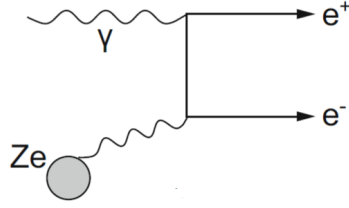


Figure 2.4: Diagram of a pair production process on a nuclei [4].

Scintillation

Scintillation is the emission of light in the characteristic wavelength of an atom or molecule due to absorbing ionising radiation. The scintillation mechanism is strongly dependent on the scintillator material. After an atom or molecule absorbs radiation of a certain wavelength, bound electrons are able to jump to higher energy states. After a certain time, the excited states relax back into the initial state by emitting a photon. In most cases the energy of this photon is less than the initial radiation as part of the energy is for example converted to phonons (heat) inside the scintillating material.

An important characteristic of a scintillator is its transparency for the light it emits itself. This effect is referred to as Stokes shift and caused by a shift between the absorption and emission spectrum of the scintillator. [4].

2.1.2 Polarisation of electromagnetic Waves

The polarisation of an electromagnetic wave is defined by the orientation of its electrical field vector

$$\vec{E} = \begin{pmatrix} E_{0x} \cdot \cos(\omega t - kz + \phi_x) \\ E_{0y} \cdot \cos(\omega t - kz + \phi_y) \end{pmatrix} \quad (2.4)$$

where ω is the angular frequency of the wave, t the time and k the wave number. Four different cases can be described:

- linear polarised: $\phi_x = \phi_y$, the direction of the vector does not change with time.
- circular polarised: $\phi_x = \phi_y \pm \pi/2$, the phase shift between the two components is 90° .
- elliptical polarised: $\phi_x = \phi_y \pm \text{const}$ with $\text{const} \neq \pi/2$, the phase shift between the two components is constant, but not 90° .
- not polarised: the direction of the vector changes randomly.

In addition, the magnetic field vector is also connected to the polarisation since it is vertical to the electric field vector [6].

2.2 Compton Polarimetry

In a Compton polarimeter, the linear polarisation is measured by using the azimuthal Compton scattering angle in scintillator arrays. A detailed description of the detection set-up by the example of the SPHiNX detector is described in Section 3.

For polarised photons, the Klein-Nishina cross section is not only dependent on the polar scattering angle θ but also the azimuthal scattering angle η with respect to the polarisation vector.

$$\frac{d\sigma_C^p}{d\Omega} = \frac{1}{2}r_e^2\epsilon^2[\epsilon + \epsilon^{-1} - 2\sin^2\theta\cos^2\eta] \quad (2.5)$$

The probability is highest for scattering perpendicular to the initial photon polarisation vector leading to a modulation in the observed azimuthal scattering angles.

fore a dependency of the number of counts in different detector units on the azimuthal scattering angle can be observed, which is displayed in the so-called "modulation curve" in Figure 2.5. From fitting a sinusoidal curve with a period of 180° to the measured counts

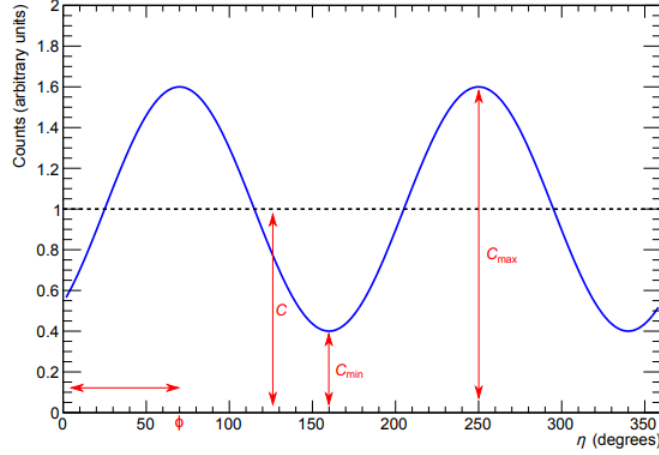


Figure 2.5: Generalised modulation curve [7].

and scattering angles, the modulation curve can be obtained and used for determining the two main polarisation parameters, the polarisation fraction Γ and the polarisation angle ϕ . The curves maximum C_{\max} and minimum C_{\min} can be used to calculate the modulation factor M

$$M = \frac{C_{\max} - C_{\min}}{C_{\max} + C_{\min}}, \quad (2.6)$$

which can then be used to define the polarisation fraction or degree Γ

$$\Gamma = \frac{M}{M_{100}} \quad (2.7)$$

where M_{100} is the modulation factor for a 100% polarised source and can be obtained through simulations. The polarisation angle ϕ is represented by the angle of the sinusoidal fit.

The Minimum Detectable Polarisation (MDP) acts as another important figure of merit for polarisation measurements and is defined for a 3σ confidence level as

$$MDP = \frac{4.29}{M_{100}R_s} \sqrt{\frac{R_s + R_b}{T}} \quad (2.8)$$

where R_s is the signal rate for polarisation event, R_b the background rate and T the observation time. It defines the lowest polarisation fraction which the detector is sensitive to at a 99% confidence level above the background [7].

2.3 Gamma-Ray Bursts as polarised Emission Sources

2.3.1 Gamma-Ray Bursts

Gamma-ray bursts (GRB's) are bright flashes of light in the energy region of 0.1-100 MeV, which randomly happen in the sky and are considered the most luminous events in the universe. Their occurrences seem to be isotropically distributed in the universe and can be observed once or twice per day. By considering the duration of these bursts, they can be grouped in two categories: short-duration bursts lasting less than 2s and long-duration bursts with a period between 2-10s [1], which can be seen in Figure 2.6.

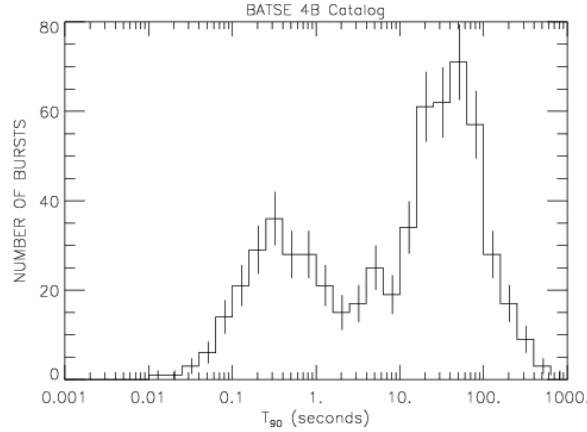


Figure 2.6: Histogram showing the population of GRBs depending on their duration. T_{90} is the time during which 5%-95% of the burst energy is emitted [8].

Long bursts are believed to be produced by so-called collapsars or hypernovas, super-massive stars which undergo a core collapse and form a black hole at the end of their lifetime. What is assumed to produce short burst are the mergers of two compact objects, for example, neutron stars or black holes [9]. The latter is strongly supported by the recent observation of a gravitational wave by the LIGO observatory together with a short GRB, which links short GRBs to neutron star mergers [2].

The spectral shape of GRBs is normally described by the so called Band function [10]

$$N(\nu) = \begin{cases} (h\nu)^\alpha e^{-\frac{h\nu}{E_0}} & \text{for } h\nu < (\alpha - \beta)E_0 \\ [(\alpha - \beta)E_0]^{\alpha - \beta} (h\nu)^\beta e^{\beta - \alpha} & \text{for } h\nu > (\alpha - \beta)E_0 \end{cases}, \quad (2.9)$$

which was phenomenological found and is not yet predicted by theoretical models. Nonetheless, it is proven to describe the observed GRB spectra excellently. In the band functions, two power laws are combined which merge smoothly at the a break energy $H = (\alpha - \beta)E_0$. The parameters α , β and the peak energy $E_p = (\alpha + 2)E_0$ are commonly used to describe different GRB spectra. Figure 2.7 shows an example of a spectral fit using the Band function.

The emission process takes place in two steps, the prompt emission of high energy gamma and X-rays and the afterglow in less energetic wavelengths (optical, radio,...), which can be explained by the fireball model. An inner engine emits shock waves at relativistic energies, the so-called "fireball". The prompt emission is believed to be produced by the interaction of these shock waves with each other due to their different

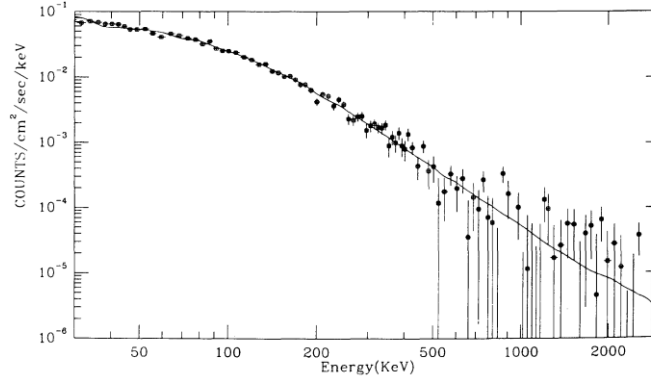


Figure 2.7: Example of a spectral GRB model fit using the Band function for the average spectrum of 1B 911177 with $\alpha = -0.968 \pm 0.022$, $\beta = -2.427 \pm 0.07$ and a break energy $E_0 = 149.5 \text{ keV} \pm 2.1$. [10].

speeds. An open riddle is the underlying process during the shock interactions which transforms the kinetic energy inside the shocks into radiation. Plausible theories are synchrotron emission, inverse Compton scattering or spectrally broadened photospheric emission. The shocks occur in the form of two jets emitted from the central engine and can only be observed if the jet direction is pointed in the direction of the observer. Through all the different internal shocks, the shock waves are slowed down and start interacting with a local external medium. These external shocks are believed to produce the less energetic afterglow following most GRBs. A schematic view of the fireball model is provided in Figure 2.8 [11].

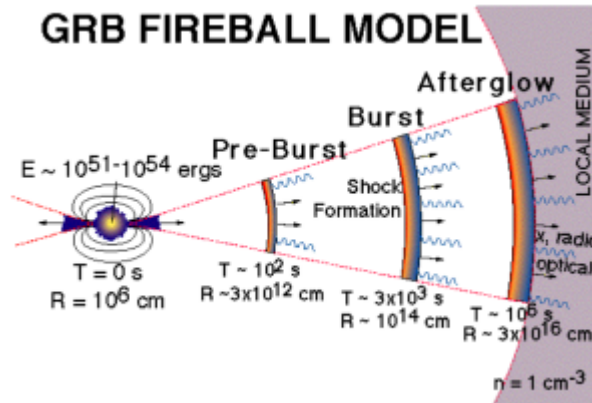


Figure 2.8: Schematic view of the fireball model for GRB emission [12].

Nonetheless, a lot of unsolved topics are connected to GRBs, such as their jet structure, jet magnetisation or the underlying emission mechanism. The three most likely radiative processes will be explained in the next section.

2.3.2 Emission Processes

The majority of emission processes leading to polarised high-energy photons are non-thermal and can lead to high degrees of linear polarisation depending on the source geometry and the magnetic fields involved. In this section, the basics of the three main

processes considered to be probable for the radiative process leading to gamma-ray bursts will be explained. How these processes appear inside GRBs and how polarisation could distinguish between the different models will be explained in detail in Section 3.1 as a motivation for the SPHiNX detector design.

Synchrotron Radiation

In the presence of a magnetic field a charged particle moving at speed \vec{v} is influenced by the Lorentz force in vacuum

$$\vec{F} = \frac{Ze}{c}(\vec{v} \times \vec{B}) \quad (2.10)$$

with Ze being the charge of the particle, c the speed of light and \vec{B} the magnetic field vector. The particle will be forced on a circular or helical path in the direction of the magnetic field dependent on the angle between \vec{v} and \vec{B} . As a result, constant acceleration is experienced by the charged particle leading to the emission of radiation.

If the particle is moving at ultra-relativistic speed, this is known as synchrotron radiation, where the relativistic framework makes it essential to distinguish between the particles rest frame and the observer frame. The synchrotron radiation is beamed into the direction of motion of the electron due to the observer frame transformation and can only be observed if the beam is in the direction of the observer. The energy spectra of electrons emitting this type of radiation in an astrophysics context are often described by power-law distributions.

The radiation from a single electron is predicted to be elliptically polarised but should transform towards linear polarisation if the energy of the electron increases, which is dependent on the pitch angle of the electron. An angle of 90° would lead to only linear polarisation being observed. The pitch angles of a crowd of electrons will be distributed and the observed beams of these electrons are within a certain angle to the line of sight. Therefore, the elliptical components of the polarisation should cancel each other out by integrating over all electron contributions and linear polarisation can be measured. It is expected to have a polarisation degree between 65%-80%, which might be reduced due to internal magnetic field structures and inhomogeneities [5].

Compton Scattering

Compton scattering was already described in Section 2.1.1. For astrophysical processes not only the classical Compton scattering is an important factor, but also the inverse process can lead to high-energy photons. During an inverse Compton scattering process, a low-energy photon scatters off a relativistic electron and is able to gain energies up to the MeV region. It leads to similar energy spectra being observed as from synchrotron radiation, which makes the distinguishing between the source processes very complicated. Both Compton and Inverse Compton scattering can produce polarised photons from unpolarised initial beams as well as depolarising initially polarised beams depending on the scattering angles as seen in Figure 2.9 [5].

Thermal Emission with spectral Broadening

One of the more recent theories predicts that the non-thermal components in the GRB emission are combined with a thermal emission explained by the photospheric model. The

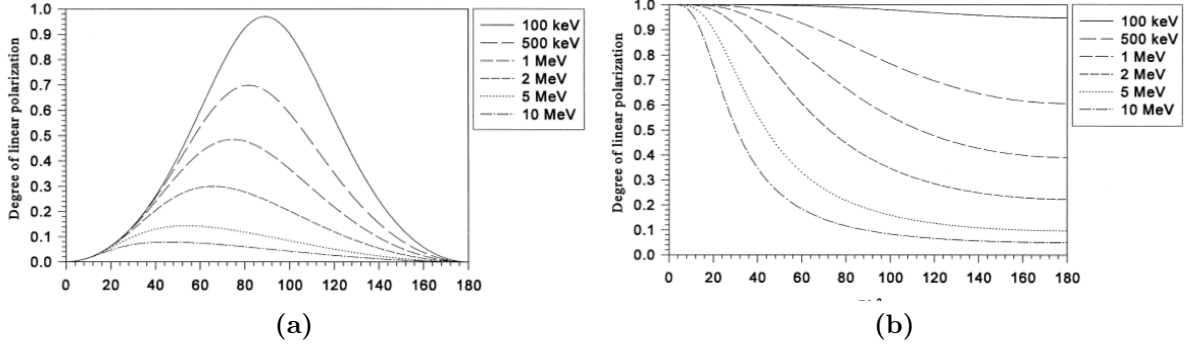


Figure 2.9: Polarisation degree of Compton scattered photons dependent on the polar scattering angle with (a) an unpolarised incident beam. (b) a 100% polarised incident beam and an azimuthal scattering angle of $\eta = 90^\circ$. Dependent on the scattering angles and the energy of the initial photon Compton scattering has a strong influence in changing the photon polarisation [5].

photosphere is the limit between opaque and transparent matter near the inner engine of the GRB. Polarised photons are produced by scatterings in the early stages of the jet and released as it expands and becomes transparent. The original thermal blackbody emission is expected to be broadened due to two possible effects: energy dissipation below the photosphere or geometric effects inside the jet.

For the first case, it is assumed that some of the internal shocks described by the fireball model are happening below the photosphere. These so-called sub-photospheric shocks lead to a "two temperatures" plasma, where one component describes the thermally distributed photons and one the hotter, scattered photons. After passing the photosphere, these photons will be emitted, resulting in a non-thermal GRB spectrum.

As a second case geometrical broadening is believed to alter the thermal spectrum, which can be explained by the "limb darkening" effect. Since the optical path of photons on-axis with the observer is smaller than the optical path of photons deviating from this path, on-axis photons are hotter than the ones observed off the line of sight. An observer is unable to distinguish the different kind of photons leading to the observation of a distorted Planck spectrum [13] [14].

Chapter 3

The SPHiNX Detector

The Satellite Polarimeter for High eNergy X-rays (SPHiNX) is a Compton polarimeter. Proposed to be launched with the second InnoSat mission in 2022 as shown in Figure 3.1, it has the purpose of measuring polarisation properties of GRBs. It is sensitive to the energy region of 50-600 keV with a timing accuracy of 100 ms and a field-of-view of 120° . Since a different mission has been chosen for the current launch, SPHiNX is left at an uncertain future [15].

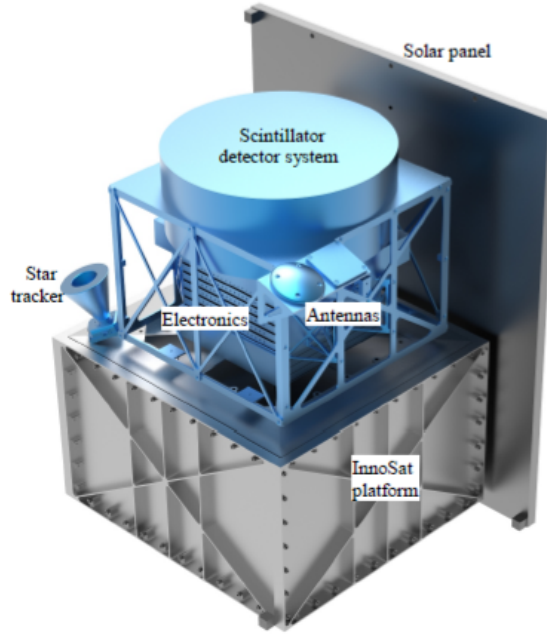


Figure 3.1: SPHiNX polarimeter mounted on the InnoSat platform [15].

This section shall give an overview of the mission and provide the basic concept ideas implemented in the simulation used for the localisation studies. First, a motivation for the SPHiNX detector will be given explaining the different scientific possibilities. Afterwards, the detector design will be discussed with the focus on the elements relevant to the localisation study. Further details concerning the mission can be found in the SPHiNX design description [15].

3.1 SPHiNX Science Goal

Even half a century after the first GRB observation, these astrophysical events remain to keep their secrets. Revealing these secrets might lay the way to detecting important astrophysical processes, such as relativistic jets, magneto-hydrodynamics, shock waves or Lorentz invariance violation.

Polarisation measurements could help to understand three aspects of the GRB emission in more detail: jet structure, jet magnetisation and the underlying emission mechanism [15].

The first dedicated polarisation mission GAP took place between 2010-2012 and was placed on the IKAROS spacecraft. It achieved to measure the polarisation of three GRBs in the 70-300 keV region, unfortunately with weak statistical significance. Nonetheless, it gave a first indication of high polarisation fractions and a 90° change in the polarisation angle for one of the bursts [16] [17].

In 2015 the CZTI instrument as part of the AstroSat mission started to observe GRBs. It is designed as a general-purpose detector but also able to pursue polarisation measurements. Again for 11 GRBs, high polarisation fractions were observed with low statistical significance [18].

The most recent mission and probably most similar to SPHiNX is POLAR, which was launched in 2016 to the Chinese space station. Unfortunately, it stopped operating after half a year due to an instrumental error. No polarisation data has yet been published, but it is expected for around 50 GRBs [19].

Nonetheless, further observations are needed to give a statistically significant result and be able to improve the knowledge about GRBs. SPHiNX is proposed as a satellite-borne instrument for hard X-ray polarimetric studies of GRBs with the aim of contributing to this kind of observations. How polarisation measurements could help to understand GRB properties is explained in the next sections, which discusses the scientific questions SPHiNX is addressing.

3.1.1 Jet Structure

As mentioned before, relativistic shock waves are emitted in the form of two jets due to an enormous energy release from the inner engine during a GRB emission. Depending on how the jets are formed and launched, their final shape can vary between being symmetric or asymmetric, wide or narrow, having a varying lateral profile or having an internal structure, for example, fragmented jets or mini-jets. By measuring the polarisation parameters, the shape of these jets could be determined. An axisymmetric jet, for instance, would lead to a polarisation parallel or perpendicular to the jet axis. Therefore, the polarisation angle would either change by 90° degrees during the prompt phase of the GRB or remain constant. Mini-jets could result in a pulsed emission from parts inside the jets, which would lead to a random fluctuation of the polarisation angle [15].

3.1.2 Jet Magnetisation

Also, the magnetic field inside the jet is yet unknown and closely connected to the main radiative emission process. One of the models for the jet emission predicts a highly magnetised plasma close to the central engine, where the magnetic fields are advected

outwards during the jet emission. This would lead to an ordered magnetic structure inside the jet resulting in synchrotron emission taking place. In this case, a maximum polarisation degree of around 50% is expected and values for the polarisation degree of around 40%.

Other models would lead to low magnetisation inside the jet, where weak magnetic field lines would vary randomly. As a result, the observed polarisation for this kind of jets would cancel each other out for an on-axis observer. For off-axis observations, a peak of the polarisation degree at 0% is expected with a tail to high polarisation degrees [15].

3.1.3 Emission Mechanism

In addition to the jet structure, the process leading to the observed highly energetic photons has not yet been revealed. Countless models exist trying to explain GRB emission, such as synchrotron radiation, emission from the jet photosphere or Compton drag models. Two possible emission cases are considered, a photospheric emission or an optically thin emission. In the photospheric case, the emission takes place close to the inner engine, where high densities of plasma and photons are dominant. If the emission takes places further away from the inner engine, where it is dominated by turbulences and shocks, it is called an optically thin emission.

In case of optically thin synchrotron radiation produced by internal shocks inside the jets, two cases can be separated. As mentioned in Section 3.1.2 the magnetic field inside the jet could be an ordered one (intrinsic model) or a random one (geometric model). Both types of magnetisation would lead to synchrotron processes taking place inside the jets as described in Section 2.3.2. For the first case, the polarisation fraction is believed to peak at around 40% with a maximum polarisation fraction of 50%. A random jet magnetisation would lead to no polarisation being observed for an on-axis observer. Nonetheless, off-axis observation could observe high polarisation degrees. The polarisation fraction would peak at 0% with a maximum of 40%. In addition, a correlation between the spectral parameter α and the polarisation fraction is expected since softer emission should lead to higher polarisation fractions.

The second case of optically thin emission is described by the Compton Drag models, where Compton scattering as explained in Section 2.3.2 is assumed as the main radiative process. The photons gain high energies by up-scattering inside the jet. Analogous to the geometric model for synchrotron radiation, the viewing angle leads to polarisation observations. However, the observed polarised emission is expected to not have any correlation with the energy spectrum in this case. The polarisation degree is expected to peak at 0% with a maximum polarisation degree of 90%.

The broadened thermal component originating from the photospheric model described in Section 2.3.2 is one of the more recent theories to describe GRB emission. Off-axis observations would show a maximum polarisation degree of around 40 % as well as a correlation between α and the polarisation degree. If energy dissipation is the broadening factor, only photons less energetic than the synchrotron peak energy will be polarised [15] [20].

Simultaneous analysis of polarisation measurements and GRB spectra could lead to a better understanding of the central emission process. The ability to separate these models by using SPHiNX is displayed in Figure 3.2. In the case of synchrotron emission with an ordered magnetic field as the main GRB source, for example, a high percentage

of the detected GRBs is expected to have a polarisation fraction of 0.3 or higher as seen in Figure 3.2 (a). This leads to the steepest line in Figure 3.2 (b) since most of the detected GRBs fulfil the criteria of $PF > 0.3$. In all of the other three cases, only the tails of the probability density distributions cause GRBs with higher polarisation fraction. Therefore the corresponding lines in Figure 3.2 (b) are less steep depending on the form of the tails since only lower percentages of the detected GRBs are predicted to show higher polarisation fractions.

With an expected observation of around 50 GRBs marked as the dashed line in Figure 3.2 (b), SPHiNX has the ability to contribute to GRB emission model separation [15].

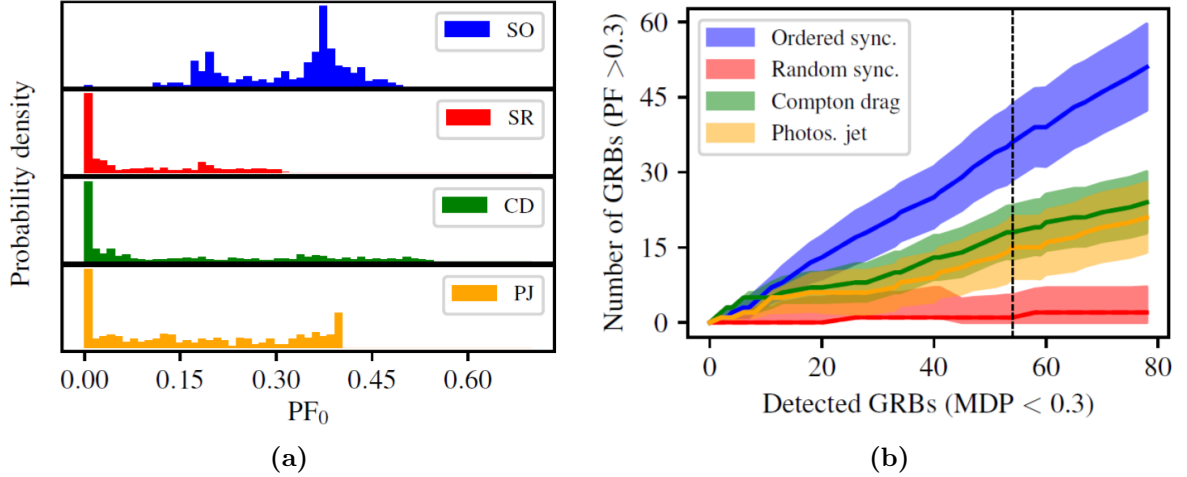


Figure 3.2: GRB emission model separation by polarisation measurements. (a) Distribution of polarisation fractions for the considered models: synchrotron emission in an ordered magnetic field (SO), synchrotron emission in a random magnetic field (SR), photospheric jet emission (PJ), and Compton drag (CD). (b) Ability of model separation at a 3σ confidence level depending of the total number of observed GRB with the SPHiNX sensitivity. Shown is a comparison between the total number of detected GRBs (x-axis) with the number of detected GRBs with a measured polarisation fraction > 0.3 (y-axis). For each model the distributions shown in (a) lead to the displayed lines and errors bars. The dashed line marks the expected sensitivity level of SPHiNX [15].

3.2 Design

The main component of the SPHiNX detector is a scintillator array as shown in Figure 3.3. Two types of scintillators are used: plastic scintillators with a low atomic number Z and therefore a high probability for Compton scattering and GAGG (Gadolinium Aluminium Gallium Garnet) scintillators with a high atomic number Z to favour photoelectric absorption. The geometry of the detector is divided into seven hexagonal units, each formed by six plastic scintillators surrounded by GAGG units. The whole array consists of 42 plastic and 120 GAGG parts. The incoming photons are expected to scatter off the inner plastic units and afterwards be absorbed inside the GAGG units. The chosen geometry enables the azimuthal scattering angle reconstruction by using two hit events inside the detector.

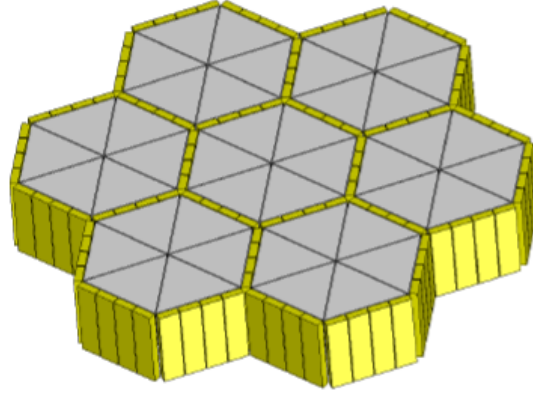


Figure 3.3: The SPHiNX scintillator array consisting of 42 plastic scintillators (grey) and 120 GAGG scintillators (yellow) [15].

For the electronic read-out, different possibilities are under discussion at the moment. The one shown in Figure 3.4 is the baseline design. Each plastic unit is read out by a single anode photomultiplier (PMT), which might be replaced by multi-pixel photon counters (MPPC) depending on further studies. MPPC read-out is also planned for each GAGG unit. The read-out signal is afterwards processed by an electronic system specially designed for this purpose. Since further optimisations are on-going and the electronic read-out as well as the processing is not included in the simulation, further details will be left for the interested reader to study [15].

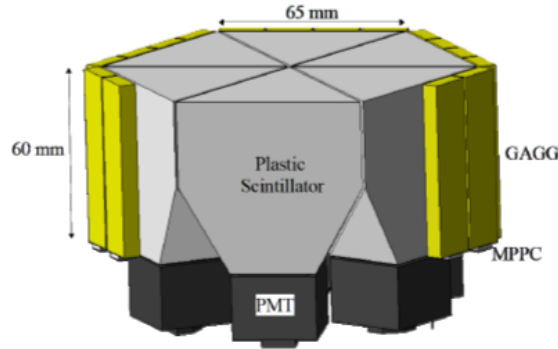


Figure 3.4: Example for one of the seven detector units of SPHiNX. Six plastic scintillators are surrounded by GAGG units and read out by PMTs [15].

A multi-layer metal shield will surround the scintillator array in order to avoid X-ray and low energy particle background. Starting from the outside, it consists of a 1 mm lead layer followed by 0.5 mm tin and 0.25 mm copper. Different geometries of the shield have been studied, either a cylindric one covering the detector from the sides and the bottom or a contour shield following the detector geometry. The different shield versions are displayed in Figure 3.5. Reasons and explanation will be given in Section 4.2. The whole structure is covered with a 1mm carbon-fibre plastic cap to protect the scintillator array and serve as additional background rejection. Mounted on the InnoSat platform one side of the covered detector is placed next to a solar panel to ensure power supply

for the detector [15].

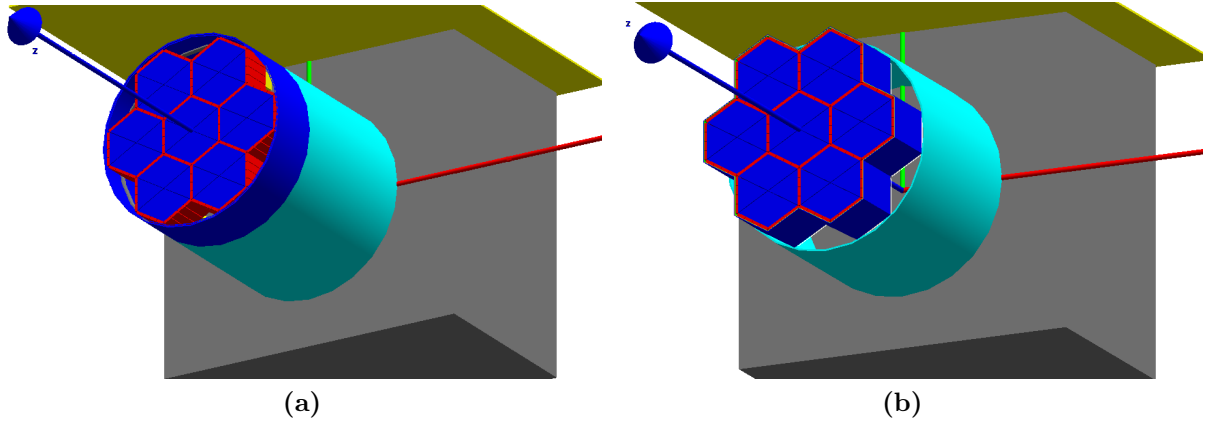


Figure 3.5: CAD model showing the SPHiNX detectors with (a) a cylindrical shield around the scintillator array. (b) a contour shield around the scintillator array. [21]

Chapter 4

Localisation Methodology

For SPHiNX to be capable of obtaining significant polarisation results, the location of the observed GRBs is a vital parameter. The localisation study in this work should be treated as a feasibility study and not a complete method for the real analysis. Therefore, different methods were designed and evaluated depending on various parameters, mainly by considering the approximations involved in each method, the computing capacities necessary and the resulting localisation precision. Momentarily, the localisation method is planned to take place offline due to limitation set by the InnoSat mission, which makes the use of more time consuming approaches possible and was considered during the study. Nonetheless, on-board localisation is in consideration to provide live GRB information for other missions.

To motivate this study, Figure 4.1 shows the increase of the MDP depending on the localisation uncertainty based on preliminary studies. The localisation uncertainty, in this case, describes the uncertainty in the polar angle since it is the main cause of changes in the polarisation results. It affects the measured polarisation fraction as well as the M_{100} and therefore the MDP. An on-axis GRB with a small polar angle causes a very distinct sinusoidal modulation curve while GRBs with higher polar angles lead to a decrease in the modulation amplitude. Since the M_{100} is determined using simulations the polar GRB position is important preliminary input information.

Figure 4.1 displays the effect the polar localisation uncertainty has on the MDP. The higher the relative increase, the less probable it is for SPHiNX to be able to determine the polarisation parameters of the affected GRBs. For uncertainties of 5° or less only around 20% of the GRBs are affected with relative MDP increases of mostly 5-15%. For higher localisation uncertainties the affected fractions are predicted to be far more with far higher MDP increases. Therefore, a localisation inside a few degrees, especially for the polar angle, is necessary for SPHiNX to provide statistically significant polarisation results.

Nonetheless, both the polar and the azimuthal angle are necessary to define the exact GRB location, which might be used for follow-up observations. Hence both coordinates are considered during the feasibility study.

As quality parameters, the offset and the uncertainty were chosen to define the reliability of the methods and the localisation itself representing the systematic and statistical errors. The offset is defined by the difference between the obtained coordinates and original GRB coordinates. For the uncertainty, the 1σ error on the obtained parameters was chosen. The coordinate system used is spherical and the considered coordinates are

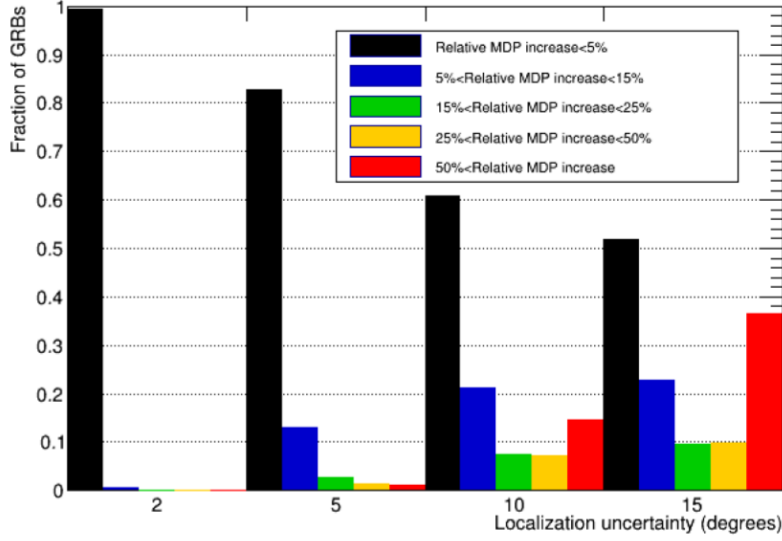


Figure 4.1: MDP uncertainty increase dependent on localisation uncertainty. A localisation uncertainty bigger than 5° starts to affect the polarimetric performance [22].

therefore the polar and azimuthal angle of the GRB position

This chapter will introduce the basic procedures applied in order to estimate the localisation capabilities of the SPHiNX polarimeter. First, the simulation set-up and data processing will be explained followed by the three different analysis methods for obtaining the localisation parameters. Some preliminary results will be mentioned to motivate decision made towards obtaining the final localisation results.

4.1 Simulation Setup

In order to be able to estimate the localisation uncertainty, simulations for different GRB positions in the sky were executed. A provided Geant4 [23] SPHiNX detector environment described in [15] [24] was used for this purpose. The different GRB spectra used in the study were implemented in the form of user-defined histograms and taken from the Fermi-GBM catalogue [25]. No polarisation was defined for the initial photons, which results in a random polarisation.

The geometric shape emitting the photons for each GRB was assumed to be a disc with a radius of 20 cm, which was chosen to cover the whole detector with arriving photons. Afterwards, the different initial GRB positions in the sky, meaning the centre of the disc, were chosen as points distributed on a sphere with 40 cm radius around the detector, which is placed at $Z = 40\text{cm}$. This was done by projecting the sphere on the x-y-plane and choosing GRB sky positions via defining X and Y. The Z coordinate was then obtained by solving the following spherical equation:

$$X^2 + Y^2 + (Z - 40)^2 = 40^2 \quad (4.1)$$

For producing databases covering the whole sky, which are necessary for some of the localisation methods, loops over X and Y were used. They were chosen to run on a unity sphere with x and y running from -1 to 1 with step sizes dependent on the methods

applied afterwards. Afterwards, x and y were scaled to X and Y by a factor of 40 cm to the sphere described by Equation 4.1. To avoid confusion the scaled coordinates will be described by capital letters X , Y , Z in this work and the unity coordinates by x , y , z .

$$x = \frac{X}{40} \quad y = \frac{Y}{40} \quad z = \frac{Z}{40} \quad (4.2)$$

Only the positive solution for z was chosen since photons are expected to enter the detector from above. If $x^2 + y^2 > 1$, meaning points outside the sphere, z was set to 0 to be able to exclude these points easily in further analysis.

The coordinate transformation for X , Y and Z is therefore

$$X = 40 \sin\theta \cos\phi \quad (4.3)$$

$$Y = 40 \sin\theta \sin\phi \quad (4.4)$$

$$Z = 40 \cos\theta \quad (4.5)$$

where θ is the polar angle and ϕ the azimuthal one.

The used grid represents the whole positive sky, which is more than the field of view proposed for SPHiNX, where the polar angle θ only runs between 0° and 60° . A schematic view of the unity coordinates used and their connection to the sky can be seen in Figure 4.2.

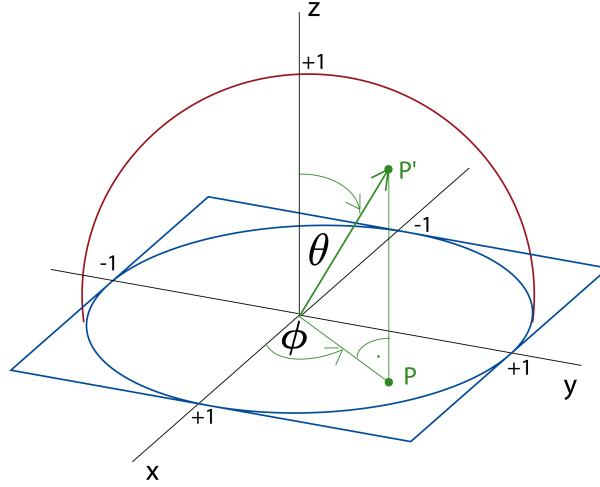


Figure 4.2: Schematic view of the used coordinate system represented by a unit sphere. The red half sphere describes the whole positive sky described by the angles θ and ϕ . The field of view of SPHiNX would be represented by the part of the sphere with $\theta \leq 60^\circ$. Each point in the x - y plane (example point P) can be uniquely connected to a point (P') on the sphere. The blue circle in the x - y plane represents the points with $x^2 + y^2 < 1$, which are used for the localisation analysis, while the blue square shows the total initial grid area.

Besides, a rotation of the GRB disc was applied dependent on the chosen X and Y . The disc's plane was rotated to be a tangent plane on the sphere normal to the vector $\vec{n} = (X, Y, Z - 40)$. This was done by providing two rotational vectors, the first one representing the new x' axis and the second one being a vector in the new $x' - y'$ -plane. For the first vector, the equation of the plane was derived by knowing its normal vector \vec{n} and a point on the plane (X, Y, Z) . Two points on this plane were chosen and subtracted

to get a vector \vec{v}_{rot1} inside the plane. Afterwards the cross product of this vector and the normal vectors was calculated with the aim of obtaining the second rotation vector $\vec{v}_{\text{rot2}} = (\vec{v}_{\text{rot1}} \times \vec{n})$. The direction of the initial photons was set to $\vec{v}_{\text{dir}} = -\vec{n}$ to reach the detector plane.

The original θ and ϕ of the GRB position can be obtained from x and y

$$\theta = \arcsin(\sqrt{x^2 + y^2}) \quad (4.6)$$

$$\phi = \arccos\left(\frac{x}{\sin\theta}\right) \quad (4.7)$$

while x, y and z can be obtained in Geant4 by getting the initial unity particle momentum and inverting its sign.

Using this method, databases equidistant in a Cartesian grid can be obtained. Figure 4.3 shows the corresponding distances in ϕ and θ for adjacent points on this grid for a step size of 0.01 in x and y .

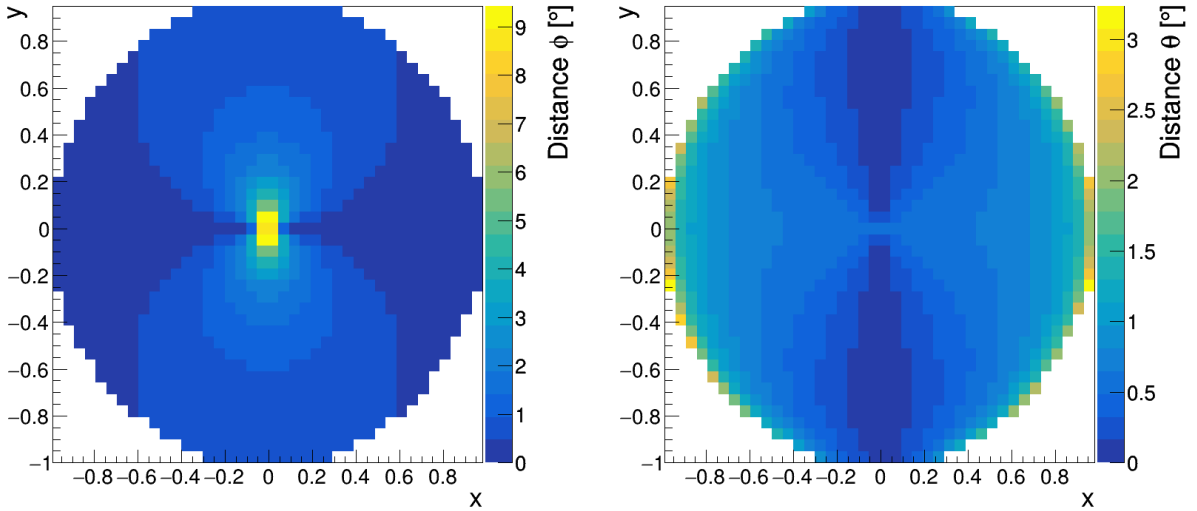


Figure 4.3: Database grid showing the distances in (a) ϕ (b) θ between adjacent points.

The number of photons started for the first simulation was either chosen to be 10^6 for the created databases, which is far more than the fluence of an average GRB, or dependent on the GRB fluences (photons/area) needed for the analysis. 10^6 initial photons correspond to a fluence of 200 ph/cm². A photon number of 10^6 was chosen since it is high enough to give a reproducible hit pattern in the detector inside the Poisson errors. Higher photon numbers would be even more suited to limit statistical fluctuations, but a compromise with computation time and capacity had to be made. GRB fluences can be grouped in the following way:

- Strong GRBs with ≈ 200 ph/cm² representing $\approx 10\%$ of all GRBs.
- Median GRBs with ≈ 20 ph/cm² representing the most common GRBs.
- Weak GRBs with ≈ 2 ph/cm² representing the weakest 20% of all GRBs.

SPHiNX is predicted to be capable of measuring polarisation for median GRBs and brighter.

In addition, the possibility of looping over θ and ϕ was implemented and the simulation set-up adapted in order to check correlations between the localisation results and the original spherical coordinates.

4.1.1 Data Processing and single Hit Selection

The output obtained from the simulation contains all of the information needed for polarisation analysis including single as well as multiple hits. A typical database used during the studies with 40400 position takes around 1.2 TB of storage space. Since most of it is not needed for the localisation, the data is processed afterwards using the data analysis framework ROOT [26]. Only certain single hits are selected and their information together with GRB properties is stored for further use. The use of only single hits makes the method independent of the polarisation properties of the GRB. This selection leads to a reduction in storage space down to 80 GB saving all information of the selected single hits.

To select the relevant hits, an event was only counted if it had more than a certain hit threshold energy. Then only single hit events were selected, which means energy deposit bigger than the hit threshold only in one detector unit. However, this means that multiple hits where less than the hits threshold energy was deposited in a second detector are still counted as single hits, which is a realistic scenario for the electronic processing. Afterwards, an upper limit for the maximal deposited energy of 600keV was applied as well as trigger thresholds for GAGG and plastic as a necessary minimal energy deposit for the single hits. The used threshold can be found in Table 4.1. The chosen trigger threshold is a compromise of background rejection and counts contributing to the statistical significance.

Table 4.1: Hit and trigger thresholds for the localisation single hit selection

	Hit threshold [keV]	Trigger threshold [keV]
GAGG	30	50
Plastic	5	50

During this step, 2D histograms displaying the number of hits per detector cell are produced to give a first impression of the obtained pattern. An example is displayed in Figure 4.4.

For the localisation studies, only the information displayed in Figure 4.4 together with the primary position is necessary assuming that spectral corrections were already taken care of. This reduces the database size to around 500 MB.

Rescaling for Energy Spectra

An important aspect is that the localisation of GRBs is known to be dependent on the GRB energy spectrum since both have an impact on the hit pattern inside the detector unit. Especially for the methods comparing test hit patterns with a preliminary produced database, the difference between the GRB spectrum used to produce the test pattern

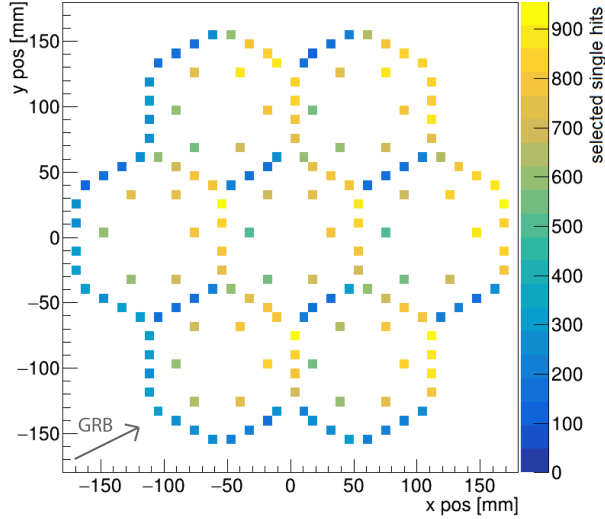


Figure 4.4: Example of a single hit pattern in the SPHiNX detector after single hit selection with a GRB placed at $\phi=-153.43^\circ$ and $\theta=63.43^\circ$. The axes describe the x and y positions inside the SPHiNX detector, while the colour legend defines the number of registered and selected hits per detector unit. The grey arrow indicates the GRB direction.

and the spectrum used for the database is expected to have a significant impact on the localisation results.

In order to be able to account for spectral dependencies, the idea was developed of using a flat energy spectrum for the initial simulation and rescaling it to the different GRB spectra afterwards. This means that later on only one database can be used for all GRB detections and scaled to the energy spectrum obtained by using the response matrix of SPHiNX obtainable during calibrations. The fact that spectral measurements are far less dependent on localisation than the other way round makes this a useful method.

For the rescaling, the GRB energy spectrum was divided in different energy bins j and for each detector unit i the counts m_{ij} were scaled to the new counts m'_{ij} by the ratio of expected to simulated spectral histogram bins

$$m'_{ij} = m_{ij} \cdot \frac{\frac{k_j^{\text{exp}}}{N_{\text{spec}}^{\text{exp}}}}{\frac{k_j^{\text{sim}}}{N_{\text{spec}}^{\text{sim}}}}, \quad (4.8)$$

where k_j is the value in the energy bin j of the expected/simulated spectrum and N_{spec} the total number of counts in the spectrum over all bins. The energy bin size was chosen to be 5 keV. By summing over all energy bins j , the number of counts per detector unit m_i used for both database method can be obtained from m_{ij} .

The spectral dependency, as well as the capability of accounting for it, is displayed in Figure 4.5. Five relevant GRBs were chosen from the Fermi-GBM catalogue [25], whose properties are displayed in Figure 4.2. Relevant in this case means GRBs, whose polarisation is predicted to be obtainable using SPHiNX.

In order to check if the rescaling can account for the energy spectrum dependency, the database created with a flat energy spectrum was scaled to two of the five GRB spectra. χ^2 minimisation as described in Section 4.3 comparing the five test GRBs with the two databases is used to evaluate the localisation uncertainty and show the different

Table 4.2: Relevant GRBs and their properties

GRB	MDP	α	β	E_p [keV]	Fluence [ph/cm ²]	t_{90} [s]
GRB140115863	0.26	-1.11	-7.41	357.04	40.98	14.909
GRB120107384	0.30	-0.94	-2.40	201.22	50.57	23.04
GRB100324172	0.11	-0.59	-5.60	445.39	170.52	17.92
GRB140721336	0.20	-1.09	-2.27	151.58	462.81	127.46
GRB090820027	0.05	-0.68	-2.60	209.45	954.17	12.416

energy dependencies. The five test files were created by simulating the relevant GRBs with their real spectra and fluences on 12 off-grid points. Both Figure 4.5 (a) and (b)

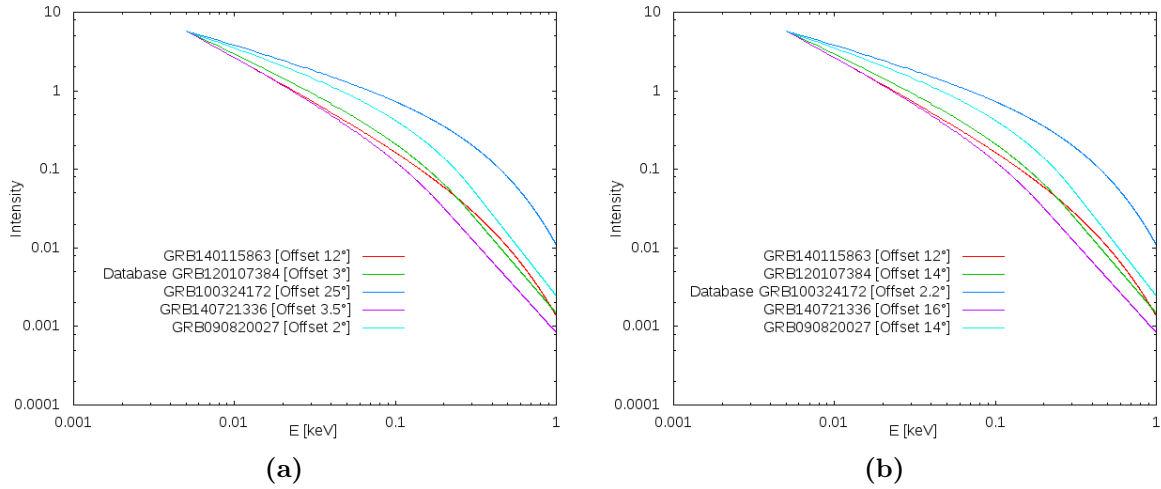


Figure 4.5: Comparison between different rescaled database spectra and four other relevant GRB spectra with logarithmic axes. The maximal offset in θ found using 12 off-grid points and χ^2 minimisation is stated for each GRB. (a) The spectrum of GRB120107384 (green) was used for rescaling the database. (b) The spectrum of GRB100324172 (darker blue) was used for rescaling the database.

show the comparison of the five different spectra in a logarithmic scale. Nonetheless, they vary in displaying the different offsets obtained in θ since Figure 4.5 (a) presents the results for rescaling the database to GRB120107384, while 4.5 (b) uses the GRB100324172 spectrum. For comparing the rescaled spectrum with the corresponding GRB test files, offsets inside 3° are observed for both same spectrum analysis. In case of using GRB test files with a non-matching spectrum, higher offsets occur. Further studies considering the dependencies on the individual spectral parameters would be necessary to understand the underlying correlation. Nonetheless, rescaling for energy spectra seems to be an useful method to enable no further spectral considerations during this localisation study.

4.2 Modulation Curve Method

As a first and rather fast approach, the "modulation curve method" was inspired by neutron background studies of the former PoGO+ detector. The main advantage of this

method is that no database needs to be produced in order to apply it and no significant impact of energy spectrum dependency is expected.

When looking at the single hit patterns in the detector, one could conclude that there might be a correlation between the original azimuthal angle and the number of hits in a detector depending on its azimuthal position. Especially in the outer GAGGs, this correlation is clearly visible. The used approach to measure the azimuthal angle of a GAGG unit is dependent on the centre of the relevant hexagonal circle making up the scintillator array as shown by the example in Figure 4.6. An alternative method is to use the centre of the whole detector ($x=0, y=0$).

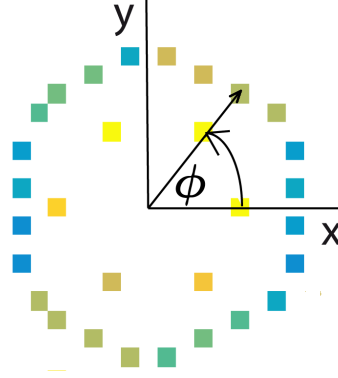


Figure 4.6: Schematic view of the azimuthal detector position by using the single hit pattern in the SPHiNX detector. Shown is one of the seven hexagonal scintillator circles. For each GAGG the centre of its individual circle is used together with the positive x axis to define the azimuthal position ϕ .

In order to evaluate this idea the number of hits in the outer GAGGs scaled by the average hit were plotted over the azimuthal detector position including Poisson errors $\sqrt{N_{\text{counts}}}$ on the data points. Afterwards the data is fitted with cosines with 360° and 180° periods

$$f(\phi) = p_2 + p_0 \cdot \cos(2(\phi + p_1)) + p_3 \cdot \cos(\phi + p_4) \quad (4.9)$$

where p_0, p_1, p_2, p_3, p_4 are the different fit parameters.

Depending on which shield is used p_1 or p_4 define the obtained azimuthal angle. For the original cylindrical shield, the 360° component is too suppressed by the different geometries and therefore only the 180° component, p_1 , can be used. This leaves two opposite directions to be chosen. Figure 4.7 (a) shows hit pattern inside the detector using the cylindrical shield and Figure 4.8 (a) the resulting modulation curve fit for the same case. By comparing the two figures, one can conclude that the region with more distance between the data points and the fit is the azimuthal direction of the GRB. Most of the incoming photons are absorbed by the tight side shield on the incoming side except for the corners, where an open area between shield and GAGG units exists. On the side not facing the incoming photons, a more uniform distribution can be seen since no interaction with the shield affects the photons. Therefore $\phi_{\text{fit}} = p_1 \pm 180^\circ$ is investigated and the angle chosen, where the distance between fit and data points is larger. Figure 4.8 (a) does not yet include error bars on the data points since it was computed at an earlier stage of the study and not repeated due to the decision described below.

The second case using a contour shield following the hexagonal shape of the detector shows both the 360° and 180° in the fit as seen in Figure 4.8 (b). The corresponding hit

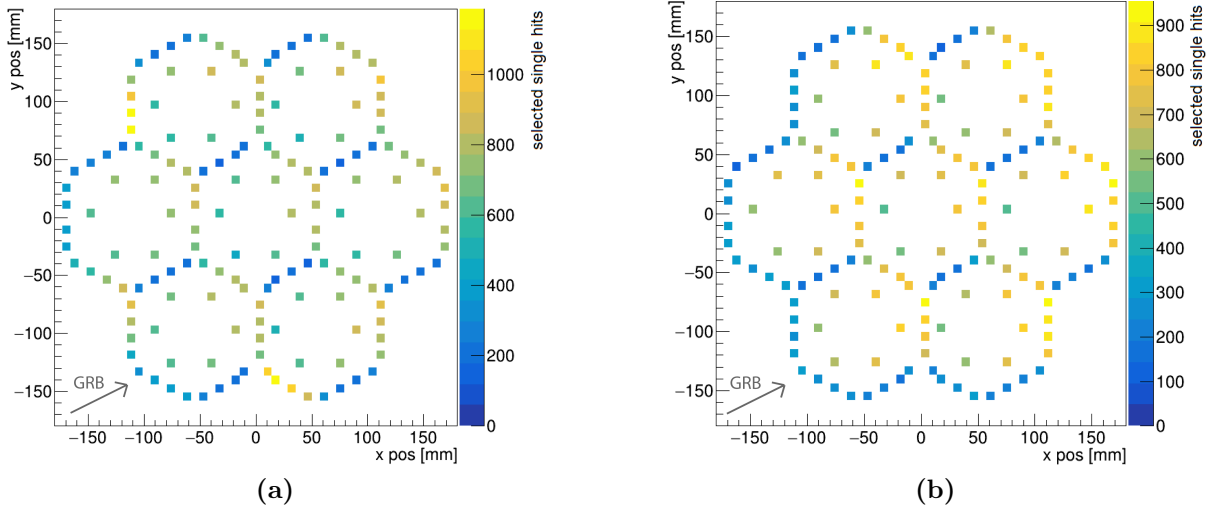


Figure 4.7: Single hit pattern with a GRB at $\phi=-153.43^\circ$ and $\theta=63.43^\circ$ using (a) a cylindrical shield around the detector. (b) a Contour shield following the detector geometry around the detector. The axes describe the x and y positions inside the SPHiNX detector, while the colour legend defines the number of registered and selected hits per detector unit. The grey arrows indicate the GRB direction.

pattern is displayed in 4.7 (b). The 360° component indicates the opposite side of the incoming photons since on the GRB facing side most photons will be absorbed by the side shield. Therefore $\phi_{\text{fit}} = p_4 - 180^\circ$ is chosen as the obtained azimuthal angle for most cases. Only if the 360° and 180° components do not match inside 10° , the 180° component is chosen since it gives more reliable results during the fitting. Then the lower peak of the fit is chosen for the azimuthal result.

Figure 4.9 compares the obtained azimuthal angles over the original ones for (a) a cylindrical shield using 121 equidistant sky positions or (b) a contour shield using 440 equidistant sky positions. Figure 4.9 (a) displays the difficulty of obtaining the true GRB direction without a 360° component, while (b) leads to the conclusion that the reconstruction of ϕ is easier done by using the contour shield. Therefore, the hexagonal shield geometry will be used for the further localisation study.

At the final stage of the study, the average of the three data points per azimuthal detector position is used for the results presented in Section 5.1 since it leads to lower χ^2 values for the individual fits by a factor of 5 even if a slight increase in uncertainties is observed.

In addition to obtaining ϕ from the modulation curve fit, θ could be retrievable from the amplitude of the 180° component p_0 . Since no clear correlation between the amplitude and the original GRB polar angle was found, a correlation dependent on ϕ and θ simultaneously was considered. The results are shown in Figure 4.10, where the dependency of the amplitude on θ is shown for a fixed ϕ . For each ϕ the corresponding θ can be found by solving $p_0 = a \cdot \sin(\theta)$, where a is obtainable by using simulations and a fit as shown in Figure 4.10.

Additionally, the possibility of background estimation was considered. It is assumed that only background fluctuations influence the localisation studies since background subtraction is planned to be used. This means that background measurement from

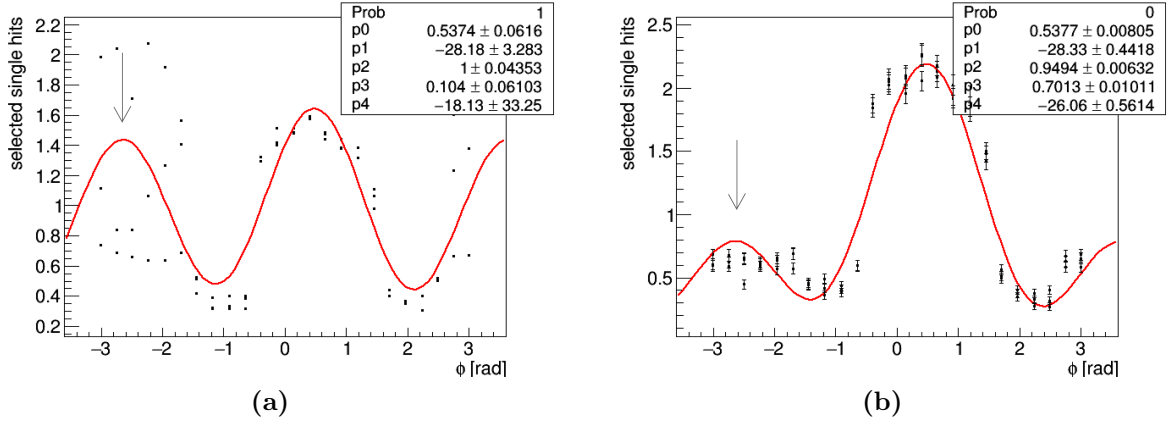


Figure 4.8: Modulation curve fits with a GRB at $\phi=-153.43^\circ$ and $\theta=63.43^\circ$ and therefore an original ϕ of -2.68 rad for (a) a cylindrical shield around the detector. Error bars on the data points are not yet included since this case was computed at an earlier stage of the study. (b) a contour shield following the detector geometry around the detector. The horizontal axis describes the azimuthal detector position while the vertical one states the selected single hits per detector unit scaled by the average hit. The selected peaks are marked by the grey arrows. The obtained fit parameters are stated as well.

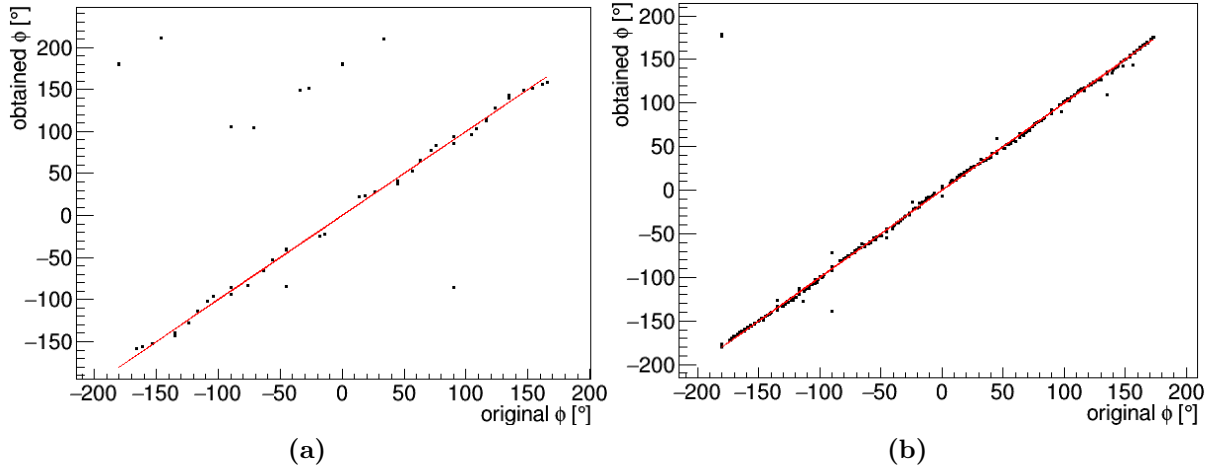


Figure 4.9: Obtained angles over original azimuthal angles using the modulation curve method and (a) its 180° component with a cylindrical shield around the SPHiNX detector. (b) its 360° component with a contour shield around the SPHiNX detector. The red lines indicates perfect reconstruction.

before and after the GRB detection will be made and subtracted from the data recorded during the GRB. Therefore, only fluctuations during the GRB duration are expected to have an impact. For the modulation curve method the background fluctuation can be included in the error bars on the data points $\sqrt{N_{\text{counts}} + N_{\text{bkg}}}$. An approximation of background hits can be computed by taking the single hit estimations for the used trigger thresholds per detector unit in the form of a rate per second [24]. The rate is then scaled to the assumed GRB durations.

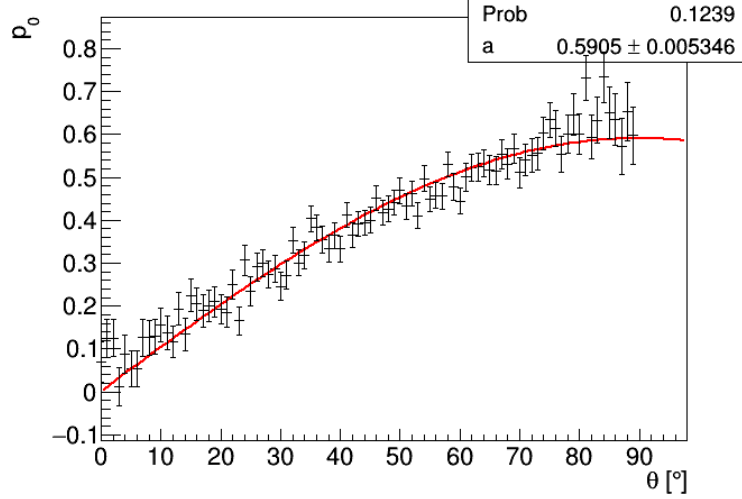


Figure 4.10: Amplitude of the 180° component of modulation curve fit dependent on θ for ϕ fixed to -63° including a sinusoidal fit used to obtain the polar angle.

4.3 χ^2 Minimisation Method

As a second approach the classical method of χ^2 minimisation was chosen. It is based and inspired by the methodology used by POLAR described in [27].

For Gaussian distributed data the classical χ^2 density for binned count data can be used to estimate the goodness of fit of a model function to the experimental data. However, many physical data sets, especially if they are obtained by Monte-Carlo simulations, follow Poisson statistics instead of Gaussian distributions. Nonetheless, an adaptation of the χ^2 density to Poisson distributed data can be made in form of Pearson's χ^2 [28] [29]

$$\chi^2 = \sum_i \frac{(c_i - m_i)^2}{m_i}. \quad (4.10)$$

where c_i are the measured counts and m_i the counts estimated by the model. In the case of SPHiNX the model counts are represented by the counts inside a database produced by the method described in Section 4.1 and compared with a test file representing the measured counts c_i . The corresponding χ^2 values can be calculated by adding over all 162 detector units in the following way

$$\chi^2(x, y) = \sum_{i=1}^{162} \frac{(c_i - c_{\text{tot}} \cdot m_i(x, y))^2}{c_{\text{tot}} \cdot m_i(x, y)} \quad (4.11)$$

where $m_i(x, y)$ is the number of counts in the detector unit i of the database file for the GRB position (x, y) scaled by the total number of counts in all used detector units for the same GRB position. c_i is the number of counts in the detector unit i for the test file and c_{tot} the total number of counts in the test sample. The test sample represents the measured GRB during the mission.

Afterwards, the minimum of the χ^2 is computed and the whole two-dimensional $\chi^2(x, y)$ grid obtained. An example of the two-dimensional distribution can be seen in Figure 4.11.

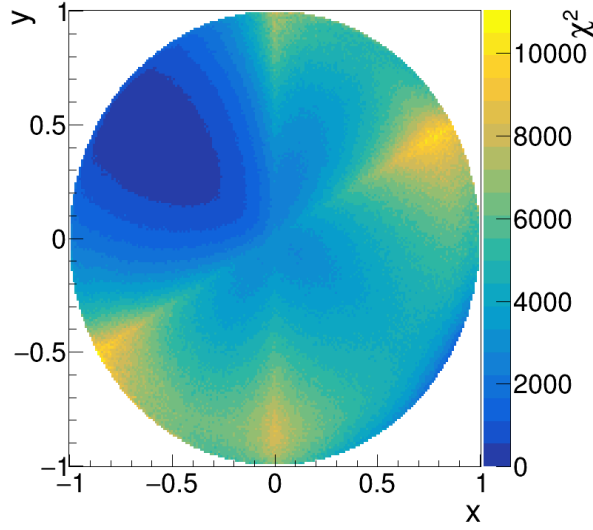


Figure 4.11: Example of a 2D χ^2 distribution with a GRB at $x=-0.58$ and $y=0.47$. The x and y axes describe the positions on the sky while the colour legend states the corresponding χ^2 values.

Different approaches were tried to find the 1σ contours leading to localisation uncertainty estimations on θ and ϕ . First contour planes of the 2D χ^2 grid at the corresponding σ levels were used to obtain the localisation results as displayed in Figure 4.12 but discarded since they were limited by the coarseness of the database grid. Nonetheless, the contours might be used for a finer grid or less steep χ^2 distribution in the case of weak GRBs. Besides, a 2D paraboloidic fit was tried to be applied to the χ^2 grid around the minimum, but the fit did not seem to represent the data well enough to give reasonable results. The final and most stable approach was to use the 1D errors on x and y to find the uncertainty on θ and ϕ through error propagation. First the x or y planes around the χ^2 minimum at (x_{\min}, y_{\min}) are examined by selecting data either at $x = x_{\min}$ or $y = y_{\min}$. This leads to 1D χ^2 distributions dependent on x or y . All data points inside a certain χ^2 limit are chosen and fitted with a 2nd order polynomial. The minimum of the obtained parabola at x'_{\min} (y'_{\min}) with a value of χ'^2_{\min} is chosen as the obtained x (y) coordinate. For the uncertainty half of the distance between the two points with a function value of $\chi'^2_{\min} + 1$ is used as 1σ uncertainty Δx (Δy).¹

Afterwards, these uncertainties are used to obtain a 1D 1σ uncertainty on θ and ϕ through error propagation.

$$x = \sin\theta\cos\phi \quad y = \sin\theta\sin\phi \quad \Rightarrow \quad \theta = \arcsin(\pm\sqrt{x^2 + y^2}) \quad \phi = \operatorname{atan}\left(\frac{y}{x}\right) \quad (4.12)$$

Only the positive sign is used to compute θ since the convention of only positive θ values has been chosen. This leads to

$$\Delta\theta = \sqrt{\frac{x^2(\Delta x)^2 + y^2(\Delta y)^2}{x^2 + y^2 - (x^2 + y^2)^2}} \quad (4.13)$$

¹To not get confused with the different coordinates:

$x_{\min}, y_{\min}, \chi^2_{\min}$...coordinates and value of the minimum in the obtained χ^2 grid

$x'_{\min}, y'_{\min}, \chi'^2_{\min}$...coordinates and value of the minimum of the fit applied to the 1D χ^2 distribution.

$x_{\text{real}}, y_{\text{real}}$...coordinates of the original starting position of the GRB

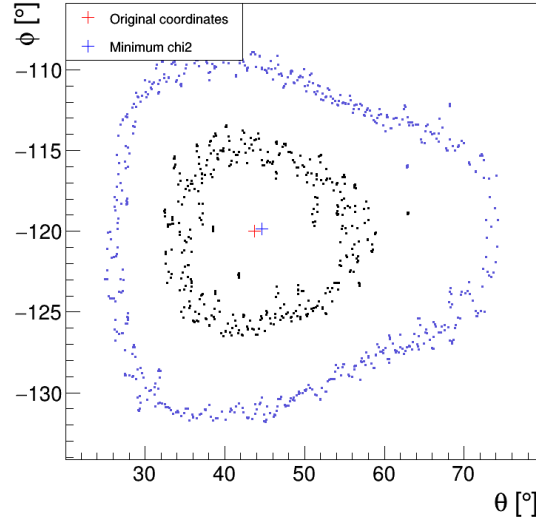


Figure 4.12: Example of a contour plot for a weak GRB using the χ^2 method. The 1σ (2σ) level is shown by the black (blue) points. The red cross marks the original GRB position and the blue cross the obtain χ^2 minima.

$$\Delta\phi = \sqrt{\frac{y^2(\Delta x)^2 + x^2(\Delta y)^2}{(x^2 + y^2)^2}} \quad (4.14)$$

By inserting x'_{\min} and y'_{\min} for x and y and the corresponding Δx and Δy the uncertainties on θ and ϕ can be obtained. Figure 4.13 displays examples of the 1D χ^2 distributions.

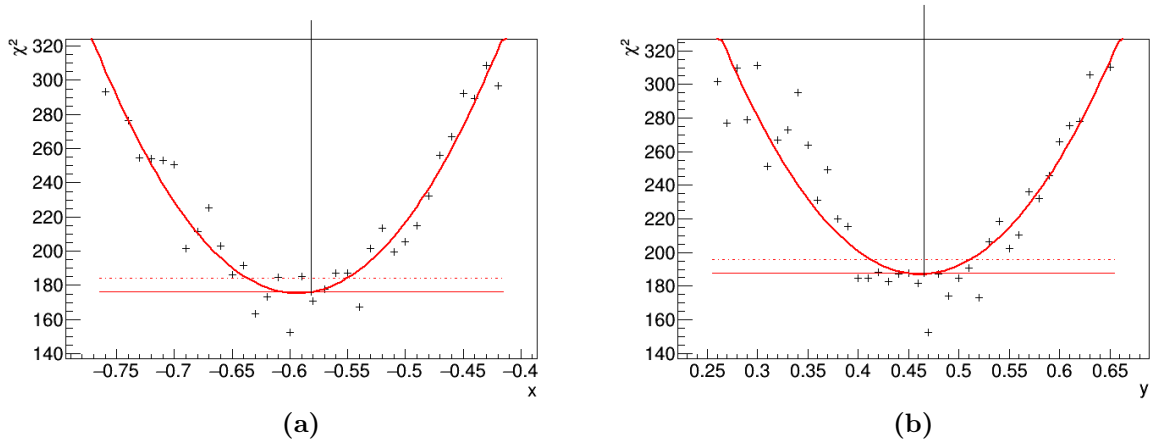


Figure 4.13: 1D polynomial fits χ^2 distribution over (a) x . (b) y . The red line marks the 1σ confidence level and the dashed red line the 3σ confidence level, while the black vertical line shows the original GRB coordinate.

An additional approach including the result of the modulation curve method intends to estimate the χ^2 dependence on θ directly. The χ^2 grid is interpolated for the line connected to the value of ϕ_{fit} obtained through the modulation curve fit. Afterwards,

the same polynomial fit as before is applied to the 1D χ^2 distribution dependent on θ as shown in Figure 4.14. The minimum of this fit is treated as the obtained θ value while $\Delta\theta$ can directly be obtained using the fit function. How the uncertainties on ϕ_{fit} can be included is a topic of future discussions and lead to the development of the maximum likelihood method.

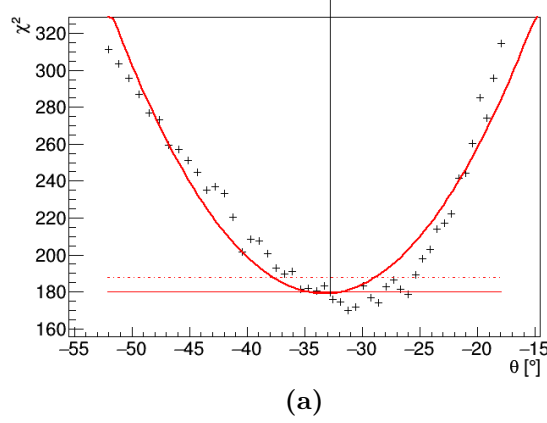


Figure 4.14: 1D polynomial fits χ^2 distribution over θ including the modulation curve result. The red line marks the 1σ confidence level and the dashed red line the 3σ confidence level, while the black vertical line shows the original GRB coordinate.

For the background cases the same assumptions as before were made, which leads to an adapted χ^2 calculation [30]

$$\chi^2(x, y) = \sum_{i=1}^{162} \frac{(c_i - c_{\text{tot}} \cdot m_i(x, y))^2}{c_{\text{tot}} \cdot m_i(x, y) + b_i(1 + r)} \quad (4.15)$$

and the same subsequent treatment as before. b_i represents the background hits per detector and $r = \frac{t_0}{t_{\text{bkg}}}$, where t_0 is the duration of the GRB and t_{bkg} the total background observation time before and after the burst. A longer t_{bkg} leads to less uncertainty on the localisation results, which will improve with each measured GRB and hence constantly during the mission.

4.4 Maximum Likelihood Method

Since the χ^2 minimisation is derived for Gaussian distributed data, maximising a likelihood function might be more suited for Poisson data analysis. Even if high enough statistics might lead to accurate results obtained via the χ^2 minimisation because the Poisson distribution converges to a Gaussian one for these cases, the probability density properties of the likelihood function have the advantage of easier analysis after obtaining the function values.

The likelihood function represents the probability of the obtained data given a specific model, in this case a database. For Poisson distributed count data this likelihood function becomes [28]

$$L_p = \prod_i \frac{m_i^{c_i}}{c_i!} e^{-m_i} \quad (4.16)$$

and for the SPHiNX detector units

$$L_p(x, y) = \prod_{i=1}^{162} \frac{[c_{\text{tot}} \cdot m_i(x, y)]^{c_i}}{c_i!} e^{-c_{\text{tot}} \cdot m_i(x, y)} \quad (4.17)$$

with the same notation as used for Equations 4.10 and 4.11. After computing the likelihood function, it is multiplied with the prior for θ and ϕ . The prior for ϕ is 4π and for θ it is expected to be $\sin\theta$, which represents the fact that the probability of a GRB occurring directly on axis can be treated as 0 and grows with larger off-axis angles. The obtained 2D likelihood distribution over x and y is then linearly interpolated to obtain a 2D distribution over ϕ and θ with a bin size of 0.5° . The bin size was chosen compared to the distances shown in Figure 4.3. After normalising both 2D distributions to 1, they can be used as probability density functions. The 1D likelihood function can, therefore, be obtained by marginalising. It means that if for example the 1D distribution over θ is evaluated, all function points with a certain θ can be integrated over ϕ to obtain an independent probability. Examples of the different 1D distributions are presented in Figure 4.15. The 1σ error can be obtained by finding the area of 68.2% around the maximum of the distribution.

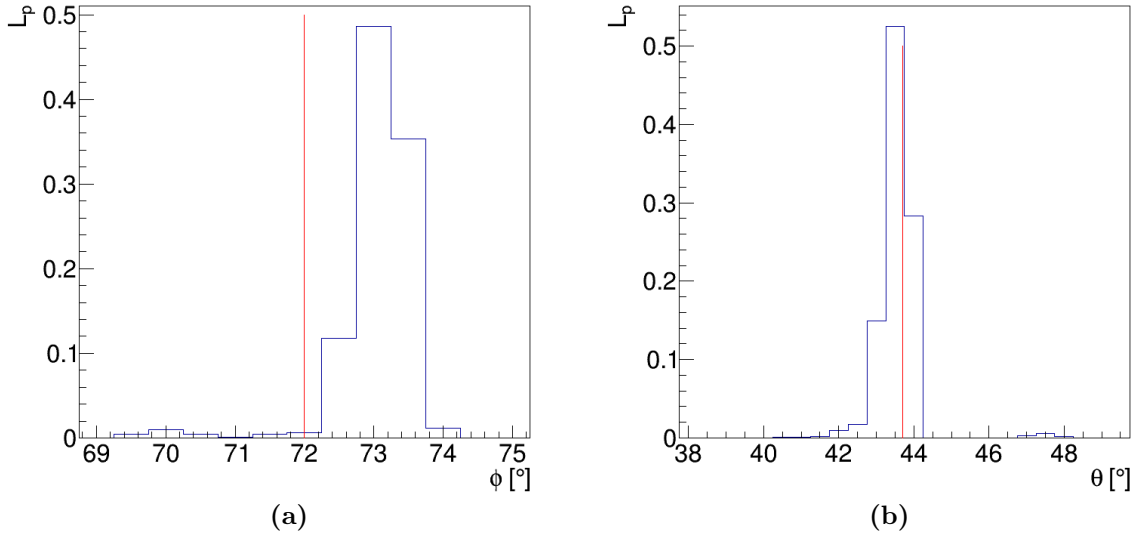


Figure 4.15: 1D maximum likelihood distributions over (a) θ . (b) ϕ . The likelihood is displayed in form of the blue histograms while the red line indicates the real GRB position.

In case of including background measurements, the Poisson distribution $p(c_i)$ in the maximum likelihood function changes to $p(s_i = c_i + b_i)$, with the same notation as used before, where $b_i = b_m$ are the average background counts during the GRB duration t_0 . The average background counts during the background observation time t_{bkg} are represented by b_T . Based on the value of $r = \frac{t_0}{t_{\text{bkg}}}$ three different likelihood functions can be defined

- The simple case of $r = 0$ with no uncertainty in the background

$$L_p = \prod_{i=1}^{162} \frac{s_m^{s_i}}{s_i!} e^{-s_m} \quad (4.18)$$

with $s_m = c_m + b_m$ and $c_m = c_{\text{tot}} \cdot m_i(x, y)$.

- The worst case scenario of $r = 1$

$$L_p = \prod_{i=1}^{162} e^{-(s_m+b_m)} \left(\frac{s_m}{b_m}\right)^{0.5c_i} I_{c_i}(2\sqrt{s_m b_m}) \quad (4.19)$$

with the modified Bessel function I_n .

- The general case of $0 < r < 1$

$$L_p = \prod_{i=1}^{162} \frac{e^{-(s_m+b_T)}}{r} \sum_{j=0}^{\infty} \frac{s_m^{c_i+j} b_T^{j/r}}{(c_i+j)!(j/r)!} \quad (4.20)$$

The background observation time will increase with GRB observations and r will therefore converge towards $r = 0$ during the mission. For a Gaussian approximation these expressions converge towards the expression in Equation 4.15 [30].

Chapter 5

Results and Discussion

The following chapter will serve to present the results of the described localisation methods. To demonstrate the reliability of each method, simulations for the GRB120107A taken from the Fermi-GBM catalogue [25] were made dependent on the three main parameters θ , ϕ and GRB fluence. For each case two of the parameters were fixed and the third one varied inside the relevant limits:

- The GRB fluence was varied from 2 - 200 ph/cm², which ranges from weak up to strong GRBs, while the other parameters were set to $\phi = -54^\circ$ and $\theta = 32.8^\circ$.
- ϕ was varied from -180 to 180°, which represents the field of view of SPHiNX, while the other parameters were set to $\theta = 43.7^\circ$ and fluence = 14.5 ph/cm².
- θ was varied from 0 to 60°, which represents the field of view of SPHiNX, while the other parameters were set to $\phi = 33^\circ$ and fluence = 14.5 ph/cm².

GRB120107A was chosen since its polarisation is expected to be obtainable by SPHiNX. In addition, it is one of the less luminous GRBs considered for SPHiNX and therefore displaying a worst case scenario.

The uncertainties and offset for all three methods considering these cases will be displayed in this chapter followed by a comparison of the different methods.

5.1 Modulation Curve Method

The first method considered is the modulation curve method. Figure 5.1 shows the obtained azimuthal uncertainty dependent on different parameters. As expected it decreases with higher GRB fluences as well as higher polar angles. An increase in GRB fluence lowers the statistical errors since higher counts are observed. The decrease with θ can be explained by more contrast in the counts in outer detector units since more photons are arriving from the sides for GRBs further off-axis. GRBs at positions with very low polar angles and therefore higher localisation uncertainties are more unlikely since they enclose only small areas of the sky compared to higher polar angle positions. For the dependency on ϕ a sinusoidal behaviour can be observed, which is due to the definition of the azimuthal detector position, which approximates the seven hexagons as circles. If the detector position is defined using the centre of the complete detector

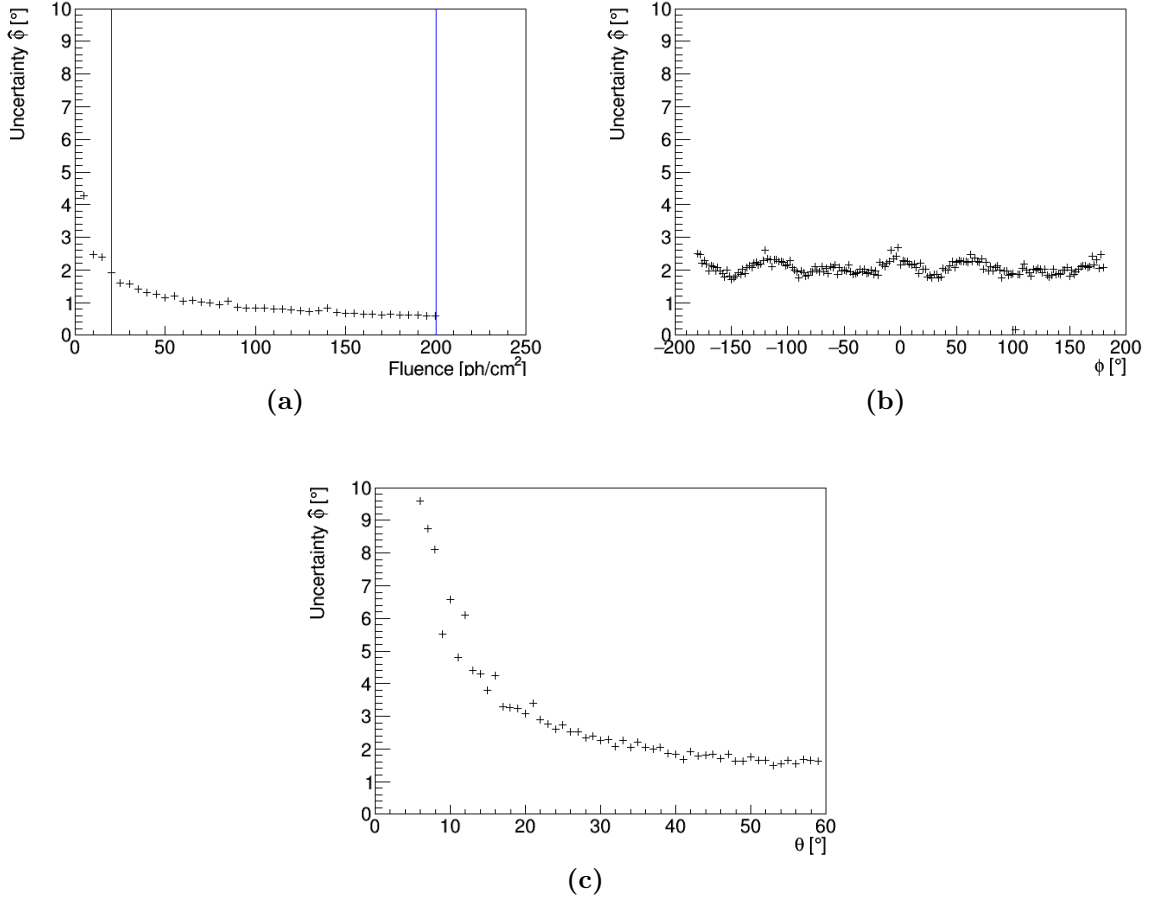


Figure 5.1: 1σ uncertainty on the obtained azimuthal angle using the modulation curve method dependent on (a) the GRB fluence with the GRB placed at $\phi = -54^\circ$ and $\theta = 32.8^\circ$. The left (right) blue line marks the fluence of median (strong) GRBs. (b) on the original azimuthal GRB position with a fixed polar GRB position $\theta = 43.7^\circ$ and a fluence of 14.5 ph/cm^2 . (c) on the original polar GRB position with a fixed azimuthal GRB position of $\phi = 33^\circ$ and a fluence of 14.5 ph/cm^2 .

as a reference frame, the sinusoidal behaviour is far more suppressed, but offsets and uncertainties increase by $\approx 30\%$.

The offsets between obtained and original ϕ are shown in Figure 5.2. For most cases, the offsets are inside the 5° level except for some outliers. However, very high offsets are observed for low polar angles. The same conclusion as for the higher uncertainty in ϕ for lower θ can be made for the offsets.

The possibility of obtaining θ using this method has not been investigated in detail, but first estimation using error propagation for including the uncertainty on ϕ showed uncertainties of $5\text{--}10^\circ$ as shown in Figure 5.3.

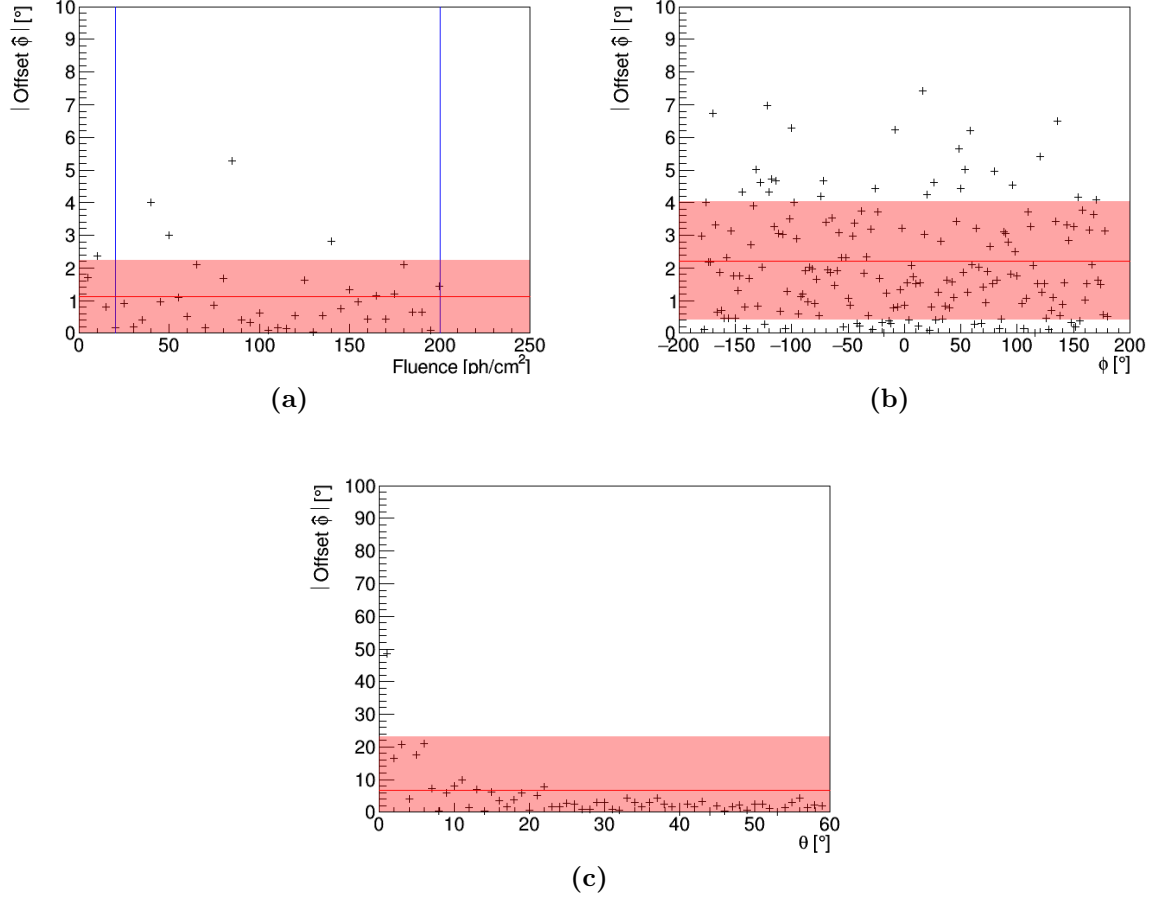


Figure 5.2: Offsets between the obtained and the original azimuthal angle using the modulation curve method dependent on (a) the GRB fluence with the GRB placed at $\phi = -54^\circ$ and $\theta = 32.8^\circ$. The left (right) blue line marks the fluence of median (strong) GRBs. (b) on the original azimuthal GRB position with a fixed polar GRB position $\theta = 43.7^\circ$ and a fluence of $14.5 \text{ ph}/\text{cm}^2$. (c) on the original polar GRB position with a fixed azimuthal GRB position of $\phi = 33^\circ$ and a fluence of $14.5 \text{ ph}/\text{cm}^2$. The red line indicates the average offset and with its standard deviation shown around it.

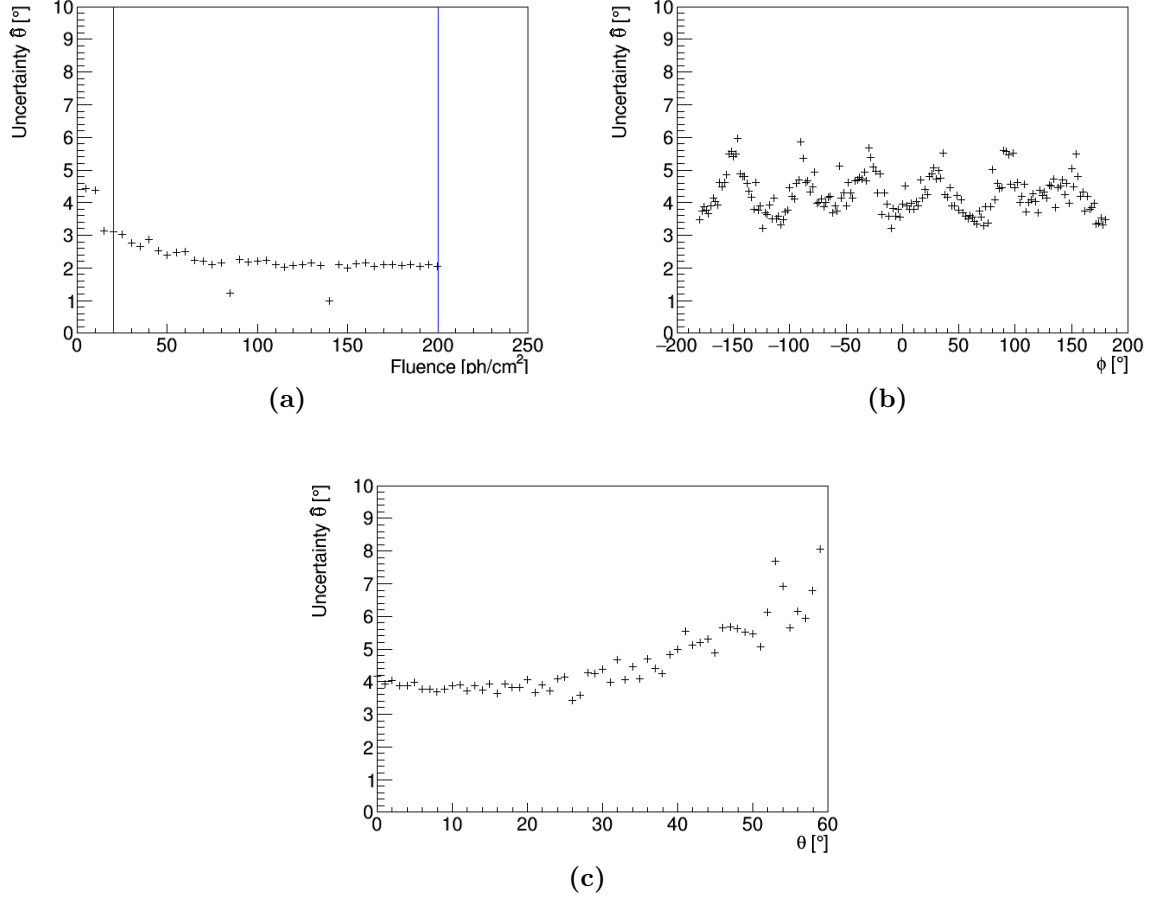


Figure 5.3: 1σ uncertainty on the obtained polar angle using the modulation curve method and error propagation dependent on (a) the GRB fluence with the GRB placed at $\phi = -54^\circ$ and $\theta = 32.8^\circ$. The left (right) blue line marks the fluence of median (strong) GRBs. (b) on the original azimuthal GRB position with a fixed polar GRB position $\theta = 43.7^\circ$ and a fluence of 14.5 ph/cm^2 . (c) on the original polar GRB position with a fixed azimuthal GRB position of $\phi = 33^\circ$ and a fluence of 14.5 ph/cm^2 .

5.2 χ^2 Minimisation Method

As a second approach, the χ^2 minimisation method is used. The data sets described above for checking the different influences are compared to a preliminary produced database scaled to the same GRB spectrum by using χ^2 minimisation as described in Section 4.3.

The results for the azimuthal localisation are presented in Figures 5.4 and 5.5. Uncertainties, as well as offsets, are inside 1 or 2°. Again lower polar angles are the exception with far higher values. This is partly correlated to the used Cartesian grid, as seen in Figure 4.3, which shows higher steps in ϕ for the central grid positions.

What should also be mentioned is the sinusoidal behaviour seen in the uncertainty with a 90° period. This is most likely due to the fact of comparing a circularly shaped test set with a Cartesian grid.

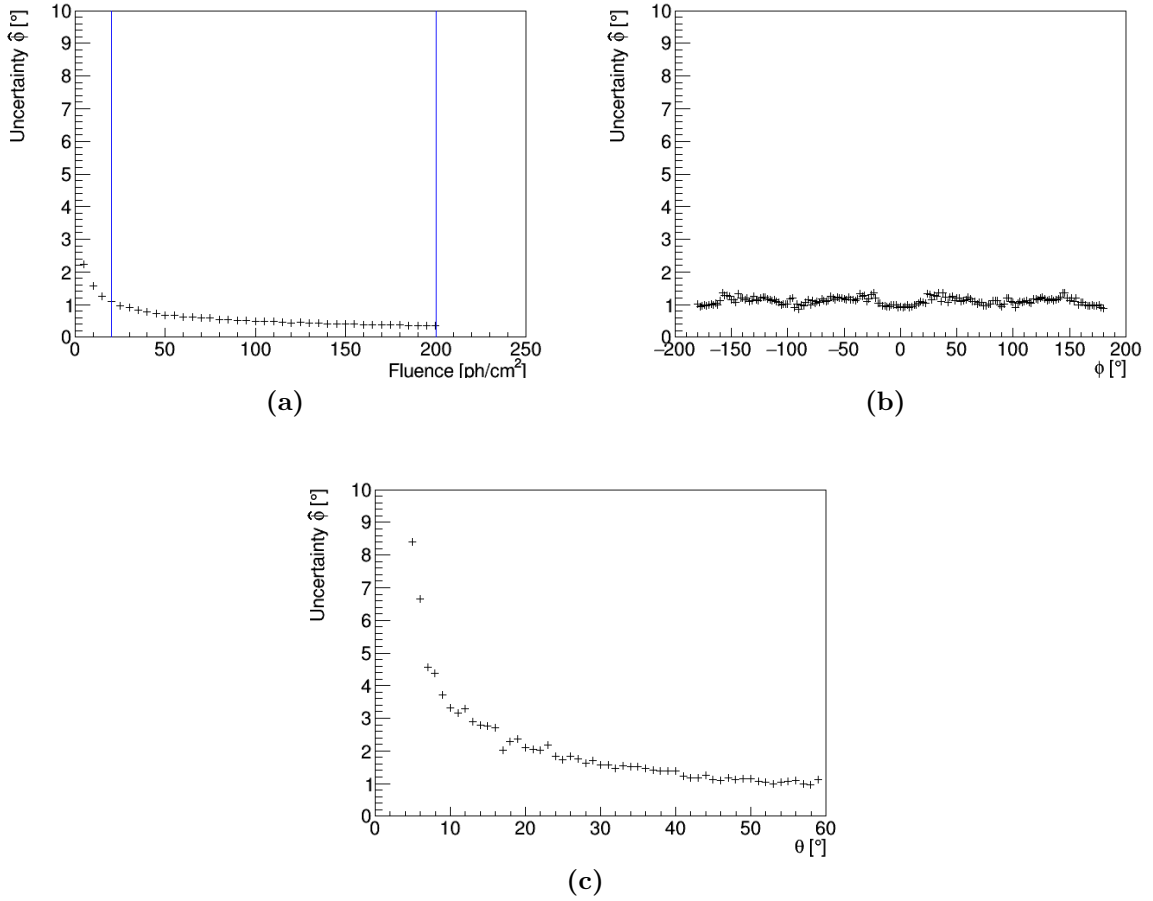


Figure 5.4: 1σ uncertainty on the obtained azimuthal angle using the χ^2 minimisation method dependent on (a) the GRB fluence with the GRB placed at $\phi = -54^\circ$ and $\theta = 32.8^\circ$. The left (right) blue line marks the fluence of median (strong) GRBs. (b) on the original azimuthal GRB position with a fixed polar GRB position $\theta = 43.7^\circ$ and a fluence of 14.5 ph/cm^2 . (c) on the original polar GRB position with a fixed azimuthal GRB position of $\phi = 33^\circ$ and a fluence of 14.5 ph/cm^2 .

Figures 5.6 and 5.7 display the localisation results for the polar angle reconstruction, which are the most relevant for the polarimetric performance. While the statistical

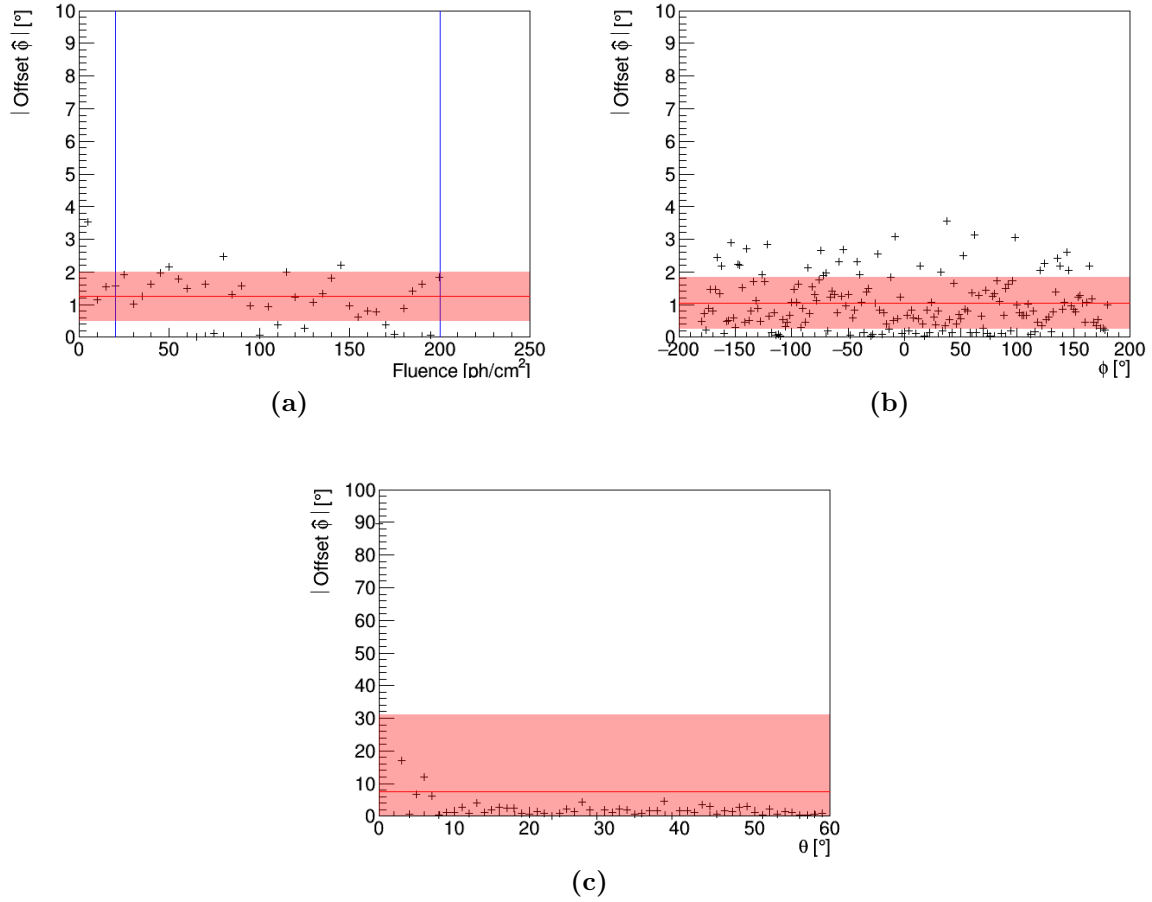


Figure 5.5: Offsets between the obtained and the original azimuthal angle using the χ^2 minimisation method dependent on (a) the GRB fluence with the GRB placed at $\phi = -54^\circ$ and $\theta = 32.8^\circ$. The left (right) blue line marks the fluence of median (strong) GRBs. (b) on the original azimuthal GRB position with a fixed polar GRB position $\theta = 43.7^\circ$ and a fluence of 14.5 ph/cm^2 . (c) on the original polar GRB position with a fixed azimuthal GRB position of $\phi = 33^\circ$ and a fluence of 14.5 ph/cm^2 . The red line indicates the average offset and with its standard deviation shown around it.

errors stay inside 2° , the systematic offsets reach a few degrees higher. Nonetheless, only a minority is outside the 5° limit. The cause of the offsets is believed to be in the Poisson fluctuations rooted in the database counts. While decreasing the photons used to produce the database by a factor of 10 an increase in average offsets on θ could be observed. Therefore, increasing the photon numbers while producing the database is believed to reduce the offsets. A slight increase in uncertainty with higher polar angles can be seen and connected to the bigger steps in θ for outer position in the Cartesian grid shown in Figure 4.3. A similar sinusoidal dependency on the azimuthal position as for the uncertainties on ϕ can be seen in the uncertainties on θ , which is also most probably caused by the use of a Cartesian grid.

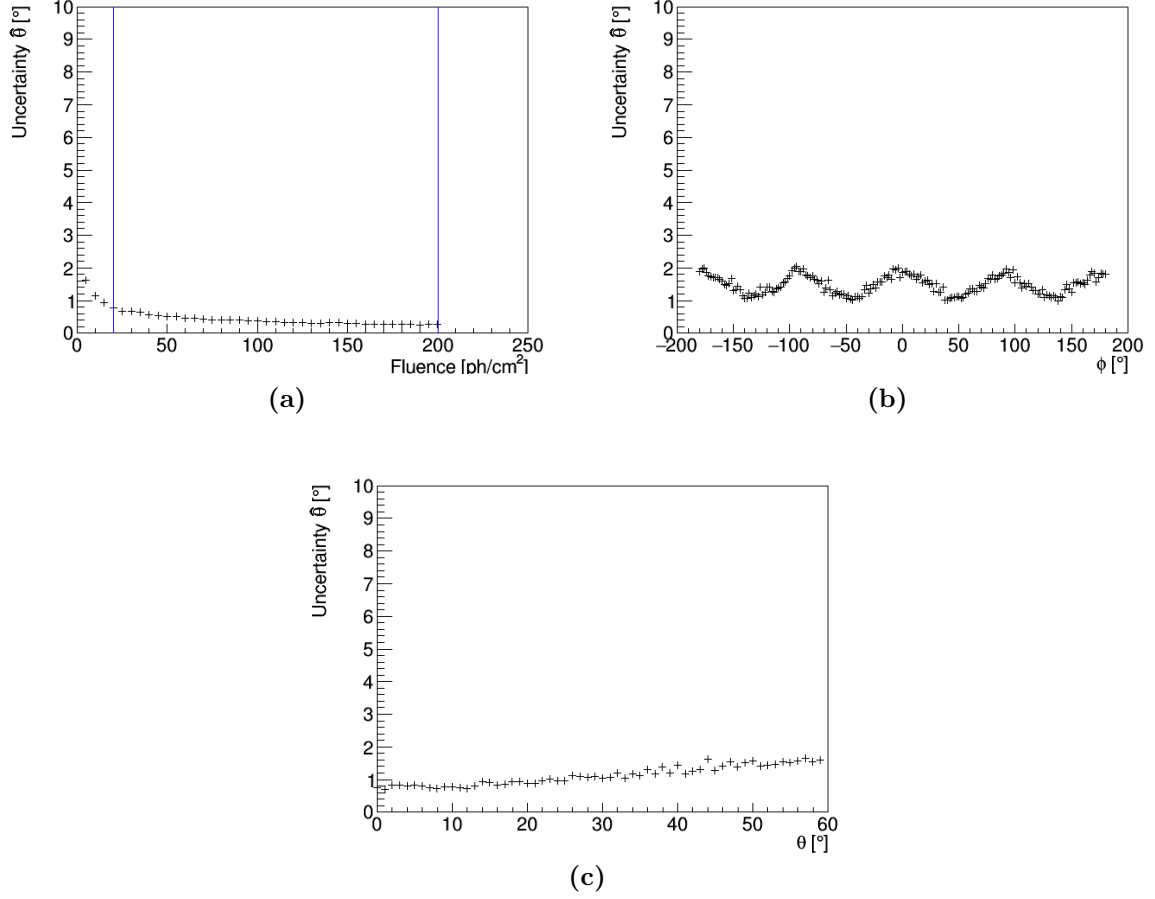


Figure 5.6: 1σ uncertainty on the obtained polar angle using the χ^2 minimisation method dependent on (a) the GRB fluence with the GRB placed at $\phi = -54^\circ$ and $\theta = 32.8^\circ$. The left (right) blue line marks the fluence of median (strong) GRBs. (b) on the original azimuthal GRB position with a fixed polar GRB position $\theta = 43.7^\circ$ and a fluence of $14.5 \text{ ph}/\text{cm}^2$. (c) on the original polar GRB position with a fixed azimuthal GRB position of $\phi = 33^\circ$ and a fluence of $14.5 \text{ ph}/\text{cm}^2$.

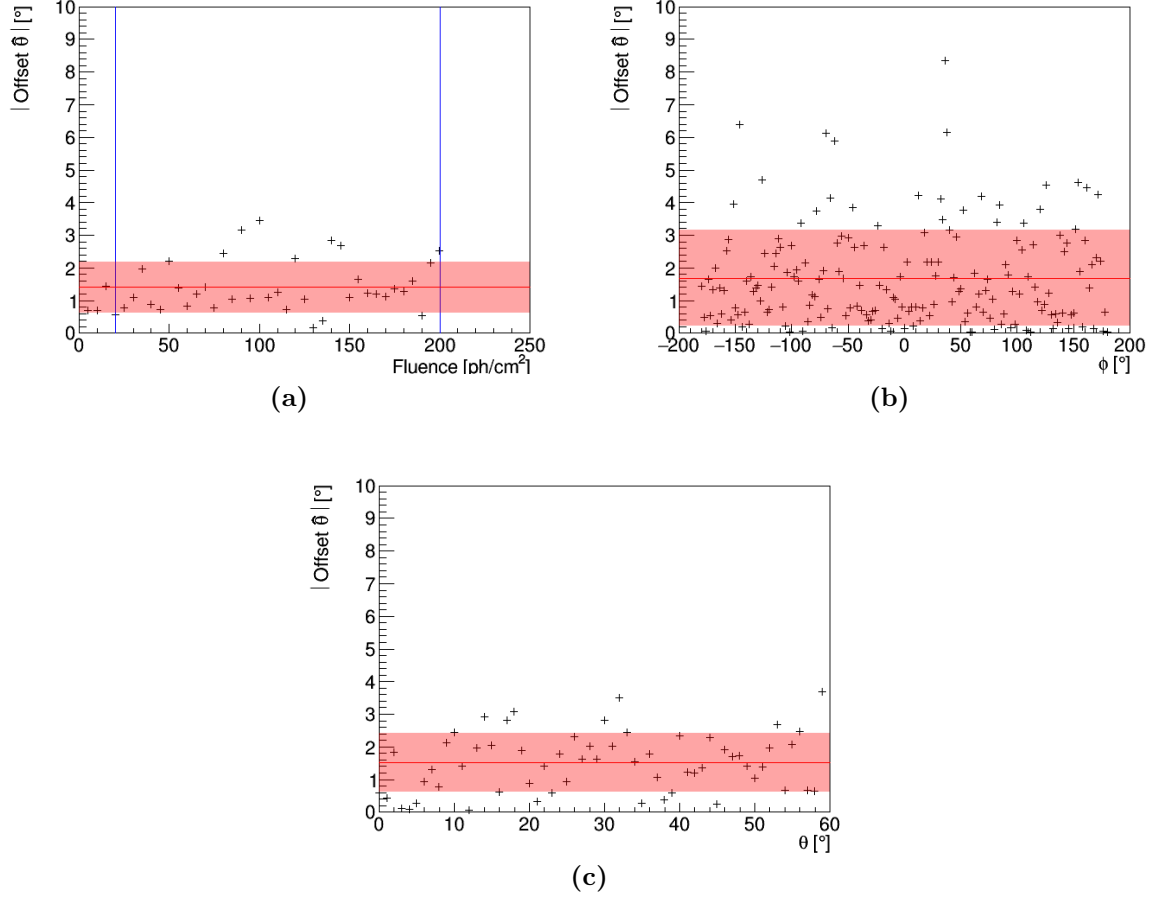


Figure 5.7: Offsets between the obtained and the original polar angle using the χ^2 minimisation method dependent on (a) the GRB fluence with the GRB placed at $\phi = -54^\circ$ and $\theta = 32.8^\circ$. The left (right) blue line marks the fluence of median (strong) GRBs. (b) on the original azimuthal GRB position with a fixed polar GRB position $\theta = 43.7^\circ$ and a fluence of $14.5 \text{ ph}/\text{cm}^2$. (c) on the original polar GRB position with a fixed azimuthal GRB position of $\phi = 33^\circ$ and a fluence of $14.5 \text{ ph}/\text{cm}^2$. The red line indicates the average offset and with its standard deviation shown around it.

5.3 Maximum Likelihood Method

As the last step, the χ^2 minimisation was replaced by a likelihood function maximisation. The same databases and test data sets as for the χ^2 methods were used. The main difference between the methods is the included prior for θ and a different procedure to estimate the uncertainties. In the case of using the likelihood function, the results are binned to steps of 0.5° due to the method described in Section 4.4.

Figures 5.8 and 5.9 show the statistical and systematic errors on ϕ , which stay inside the 5° limits except for low polar angles.

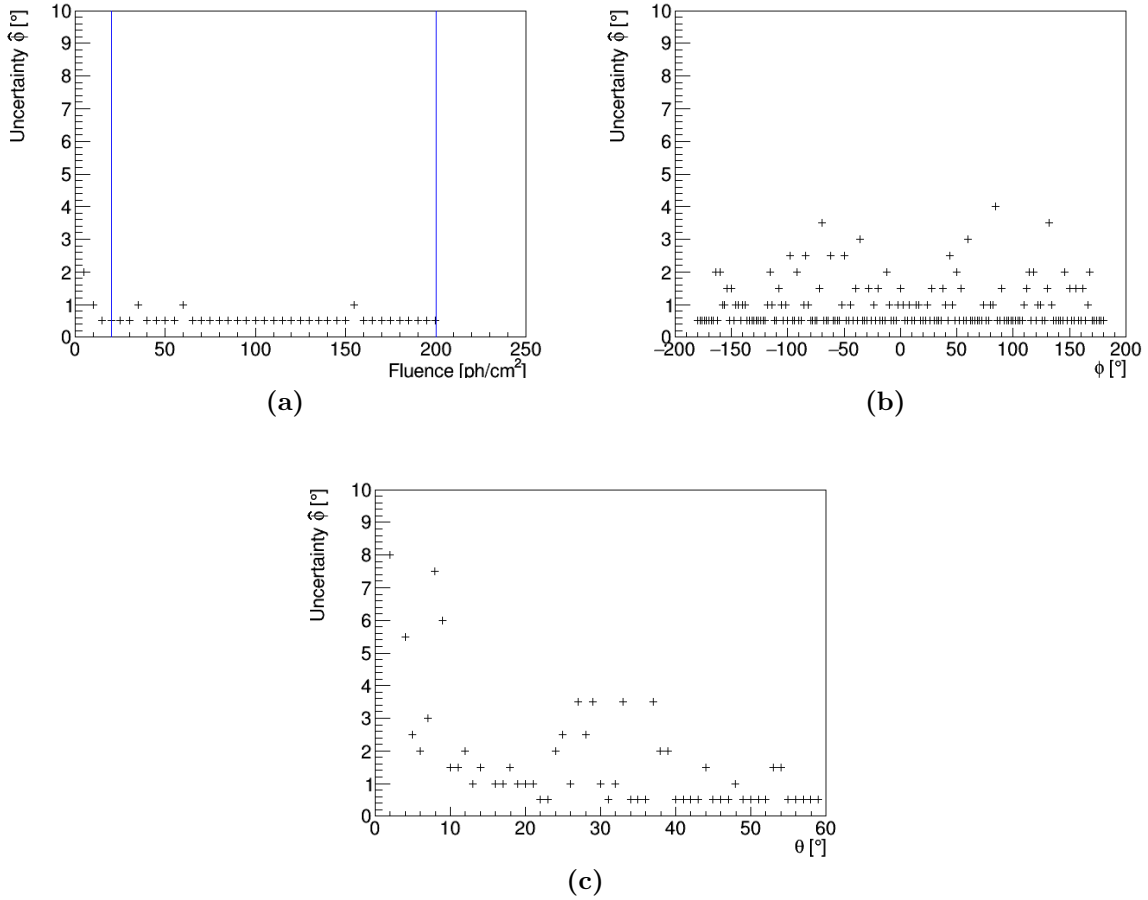


Figure 5.8: 1σ uncertainty on the obtained azimuthal angle using the maximum likelihood method dependent on (a) the GRB fluence with the GRB placed at $\phi = -54^\circ$ and $\theta = 32.8^\circ$. The left (right) blue line marks the fluence of median (strong) GRBs. (b) on the original azimuthal GRB position with a fixed polar GRB position $\theta = 43.7^\circ$ and a fluence of $14.5 \text{ ph}/\text{cm}^2$. (c) on the original polar GRB position with a fixed azimuthal GRB position of $\phi = 33^\circ$ and a fluence of $14.5 \text{ ph}/\text{cm}^2$.

Similar conclusions can be made for the results on θ as shown in Figures 5.10 and 5.11, except that the offsets show more outliers in their random fluctuation than for ϕ . The similarity to the systematics obtained from the χ^2 method supports the claim that the cause of the offsets is rooted in the statistical fluctuations of the database.

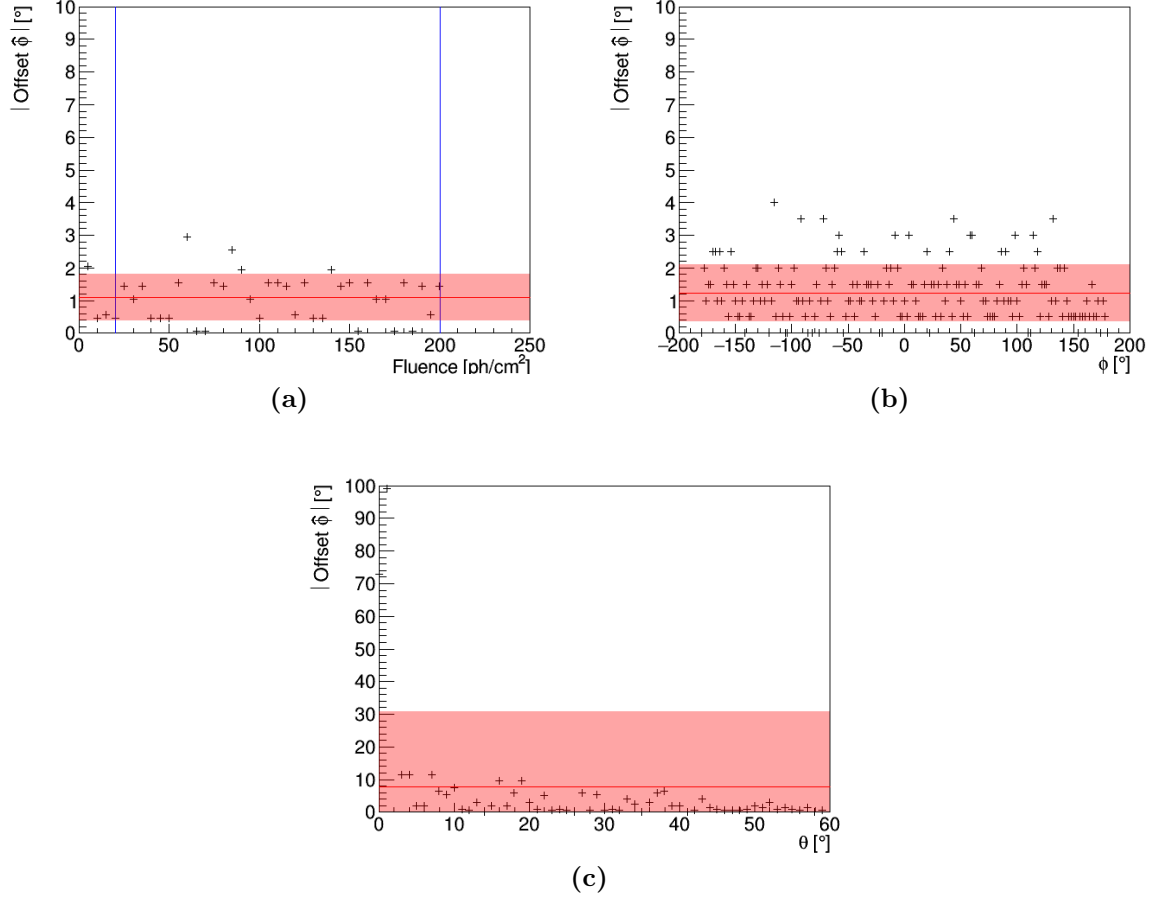


Figure 5.9: Offsets between the obtained and the original azimuthal angle using the maximum likelihood method dependent on (a) the GRB fluence with the GRB placed at $\phi = -54^\circ$ and $\theta = 32.8^\circ$. The left (right) blue line marks the fluence of median (strong) GRBs. (b) on the original azimuthal GRB position with a fixed polar GRB position $\theta = 43.7^\circ$ and a fluence of $14.5 \text{ ph}/\text{cm}^2$. (c) on the original polar GRB position with a fixed azimuthal GRB position of $\phi = 33^\circ$ and a fluence of $14.5 \text{ ph}/\text{cm}^2$. The red line indicates the average offset and with its standard deviation shown around it.

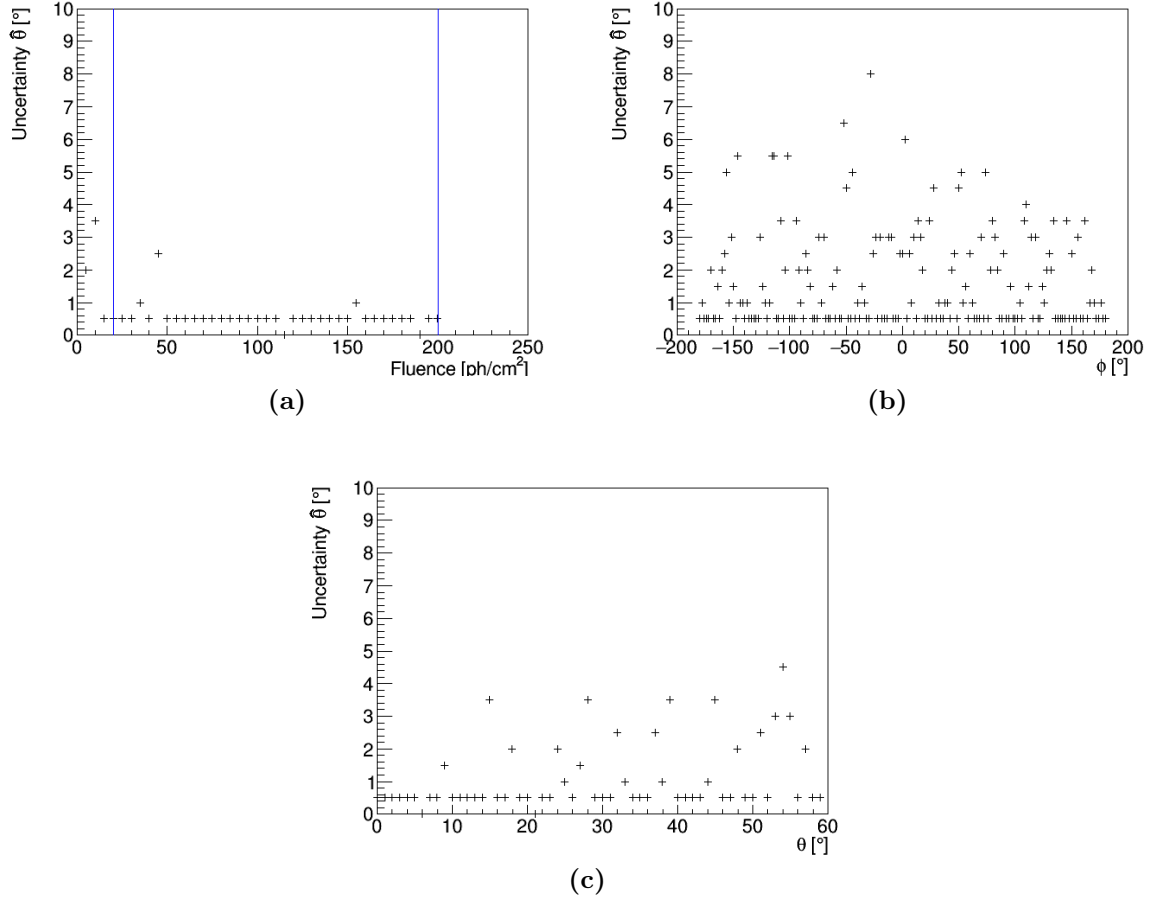


Figure 5.10: 1σ uncertainty on the obtained polar angle using the maximum likelihood method dependent on (a) the GRB fluence with the GRB placed at $\phi = -54^\circ$ and $\theta = 32.8^\circ$. The left (right) blue line marks the fluence of median (strong) GRBs. (b) on the original azimuthal GRB position with a fixed polar GRB position $\theta = 43.7^\circ$ and a fluence of $14.5 \text{ ph}/\text{cm}^2$. (c) on the original polar GRB position with a fixed azimuthal GRB position of $\phi = 33^\circ$ and a fluence of $14.5 \text{ ph}/\text{cm}^2$.

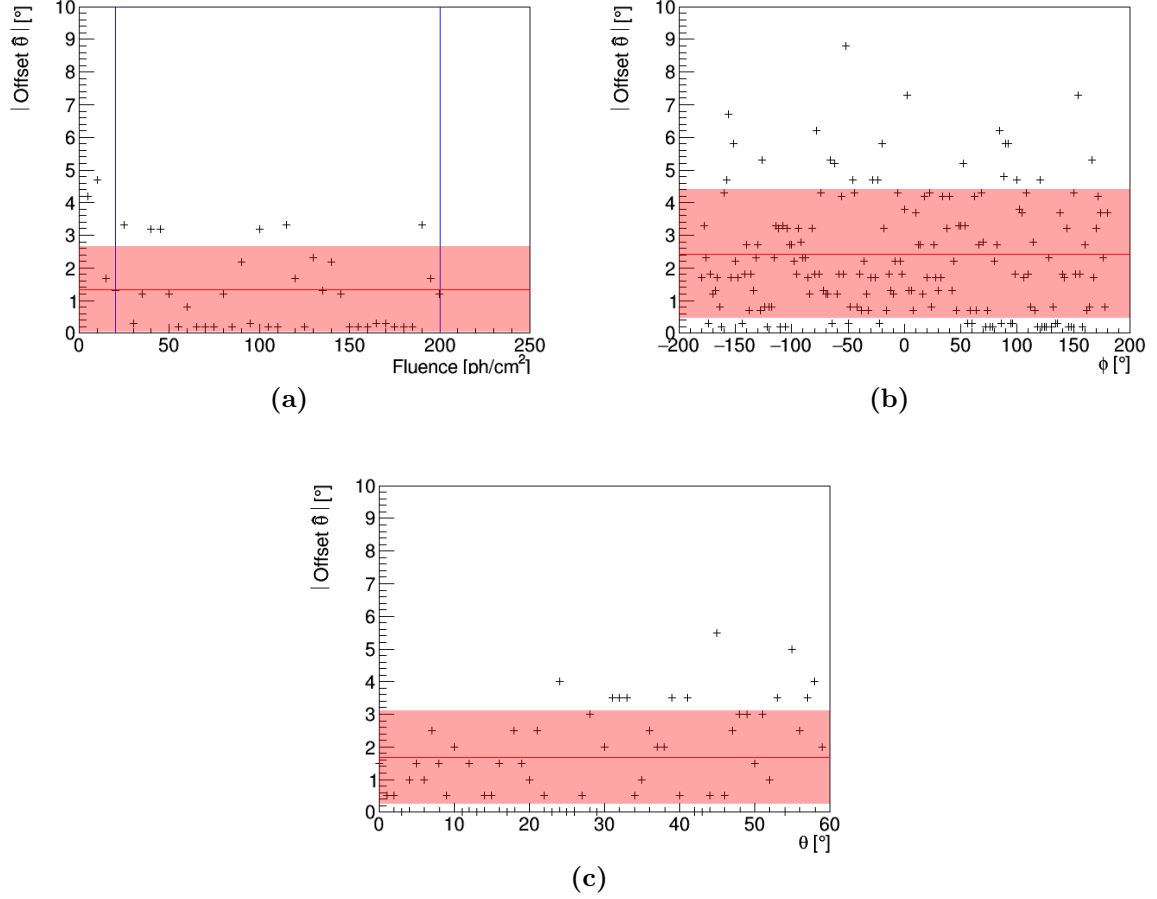


Figure 5.11: Offsets between the obtained and the original polar angle using the maximum likelihood method dependent on (a) the GRB fluence with the GRB placed at $\phi = -54^\circ$ and $\theta = 32.8^\circ$. The left (right) blue line marks the fluence of median (strong) GRBs. (b) on the original azimuthal GRB position with a fixed polar GRB position $\theta = 43.7^\circ$ and a fluence of $14.5 \text{ ph}/\text{cm}^2$. (c) on the original polar GRB position with a fixed azimuthal GRB position of $\phi = 33^\circ$ and a fluence of $14.5 \text{ ph}/\text{cm}^2$. The red line indicates the average offset and with its standard deviation shown around it.

5.4 Method Comparison

Considering the computing capacities, all three methods were tested on the same example in order to compare their computing times. The by far fastest one is the modulation curve method with 0.4s, while both database methods take around 40s. In addition, no database is necessary for the modulation curve methods, which save storage space as well as a week or more of computation time.

By comparing the results of all three methods, it can clearly be seen that the modulation curve method gives far higher systematic offsets and uncertainty. Not all of the detector information is used for this method since only the outer detector units are used and hence less statistical significance is expected. Nonetheless, it is suited as a fast first approximation with the purpose of limiting the database search and production for the other methods, which has the potential of saving computation time and capacities. In the case of including an on-board localisation algorithm, the fast computation time of this method makes it a convenient choice.

Both database methods consume more time and computing capacities than the modulation curve method but lead to more precise results. One additional point is that both angular coordinates are easily obtainable using these methods.

Comparing the χ^2 minimisation and maximum likelihood methods, the χ^2 minimisation seems to be the most suited for obtaining localisation results inside a few degrees. Far less uncertainty on θ is obtained by using the χ^2 minimisation instead of the likelihood maximisation. This is due to the very steep behaviour of the likelihood function, which is poorly described by a grid with the current step size. The χ^2 method has the advantage of using a parabolic fit to interpolate the binned grid data as well as an easier background estimation. However, it introduces additional errors due to the fact of using error propagation and by being optimised for Gaussian instead of Poisson data. The last point might have an influence on GRB localisation with low GRB fluences.

If more precise localisation is required and the capacities for using a very fine grid are available, the likelihood method is predicted to be more suited since it involves fewer assumptions introducing new errors. In addition, the fact of using it as a probability density function provides easy implementation of initial information about the GRB position. However, including background fluctuation are complicated to implement and would probably drastically increase the computation time.

5.5 Estimations including Background

To give a first estimation of the localisation results behaviour dependent on the background fluctuation, the χ^2 method together with a background observation time of 300s was used. For the duration of the GRB, the original $t_{90} = 23.04$ of GRB120107384 was used. No influence on the systematic offset in θ or ϕ could be seen. However, the uncertainties show an increase by a factor of 2 or 3 with included background as shown in Figures 5.12 and 5.13. However, they mostly fluctuate inside the 5° limit, especially for θ .

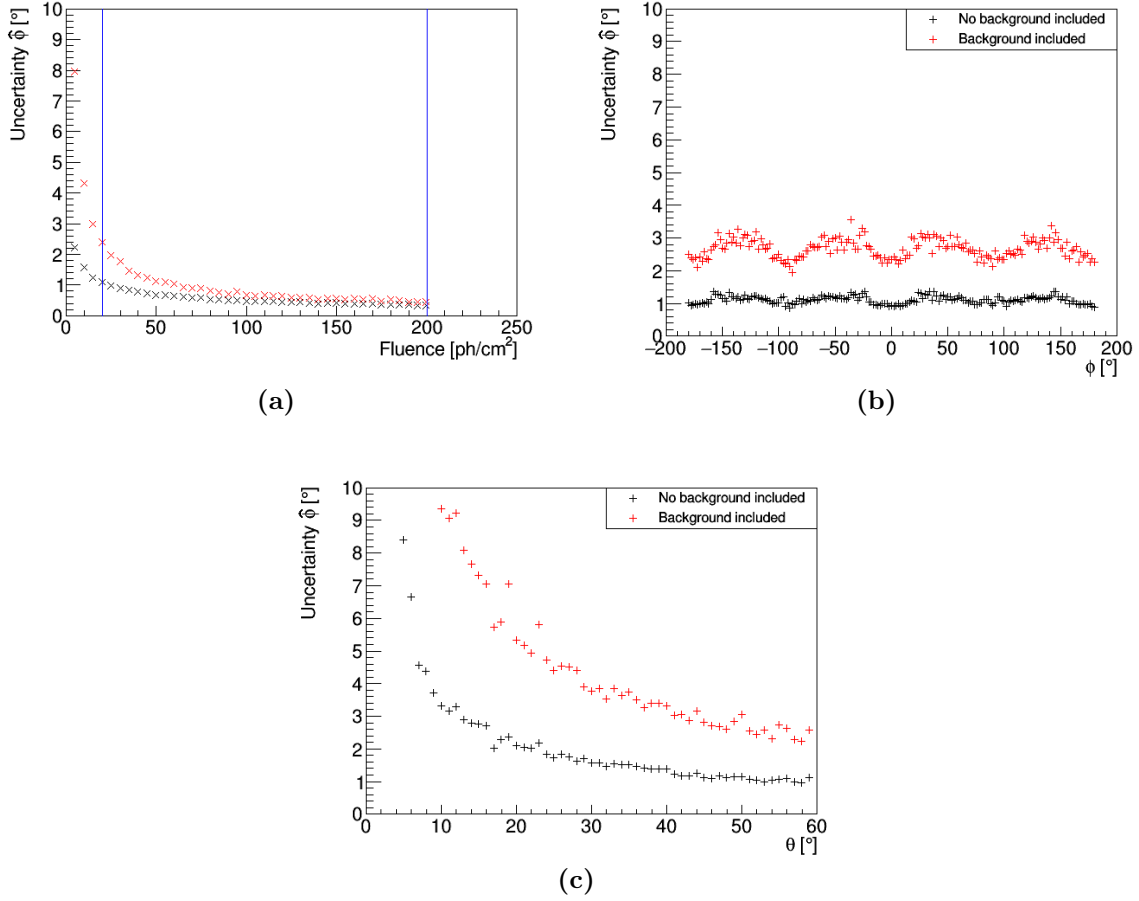


Figure 5.12: Dependency on background fluctuations ($t_{\text{bkg}} = 300\text{s}$, $t_0 = 23.04\text{s}$) of the 1σ uncertainty on the obtained azimuthal angle using the χ^2 minimisation method dependent on (a) the GRB fluence with the GRB placed at $\phi = -54^\circ$ and $\theta = 32.8^\circ$. The left (right) blue line marks the fluence of median (strong) GRBs. (b) on the original azimuthal GRB position with a fixed polar GRB position $\theta = 43.7^\circ$ and a fluence of $14.5 \text{ ph}/\text{cm}^2$. (c) on the original polar GRB position with a fixed azimuthal GRB position of $\phi = 33^\circ$ and a fluence of $14.5 \text{ ph}/\text{cm}^2$.

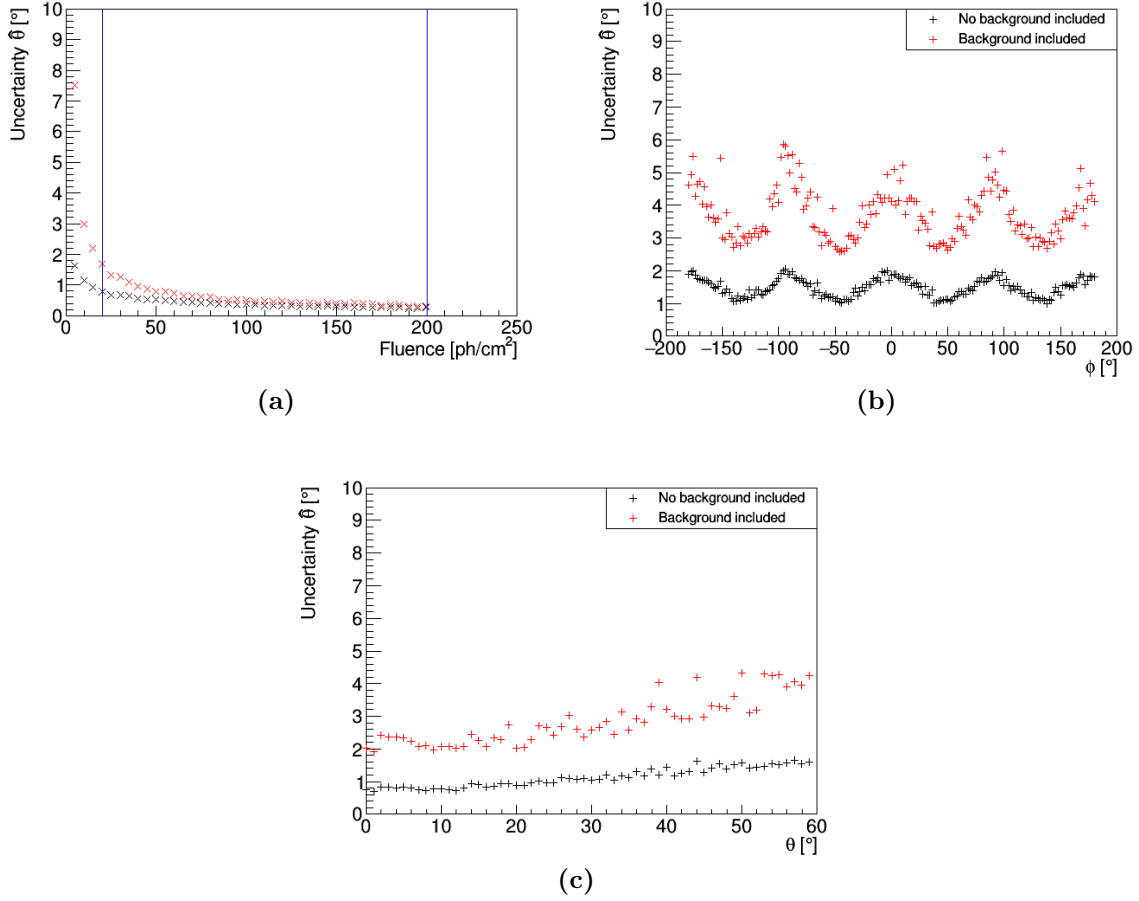


Figure 5.13: Dependency on background fluctuations ($t_{\text{bkg}} = 300\text{s}$, $t_0 = 23.04\text{s}$) of the 1σ uncertainty on the obtained polar angle using the χ^2 minimisation method dependent on (a) the GRB fluence with the GRB placed at $\phi = -54^\circ$ and $\theta = 32.8^\circ$. The left (right) blue line marks the fluence of median (strong) GRBs. (b) on the original azimuthal GRB position with a fixed polar GRB position $\theta = 43.7^\circ$ and a fluence of 14.5 ph/cm^2 . (c) on the original polar GRB position with a fixed azimuthal GRB position of $\phi = 33^\circ$ and a fluence of 14.5 ph/cm^2 .

5.6 Total localisation uncertainty

The main reason to distinguish between the polar and azimuthal component in the localisation results is the strong dependency of the polarimetric performance on θ . Even though the polarimetric performance is the main motivation for this work, the total localisation uncertainty should be mentioned as well. Nowadays many GRB missions serve to provide GRB information to enable follow-up observations and are therefore specialised in determining GRB location and spectrum with far higher precision than SPHiNX will be able to reach. However, due to the large field of view of SPHiNX, its localisation results might be useful if no other observations of the same GRB were made.

To express the total localisation uncertainty the error radius $\delta\psi$ can be defined

$$2\pi(1 - \cos(\delta\psi)) = \sin(\phi)\sigma_\theta\sigma_\phi \quad (5.1)$$

using the polar and azimuthal uncertainties σ_θ , σ_ϕ with the advantage of also being defined at $\theta = 0$ [22]. It represents the opening angle of the cone connected to the solid angle of σ_θ and σ_ϕ .

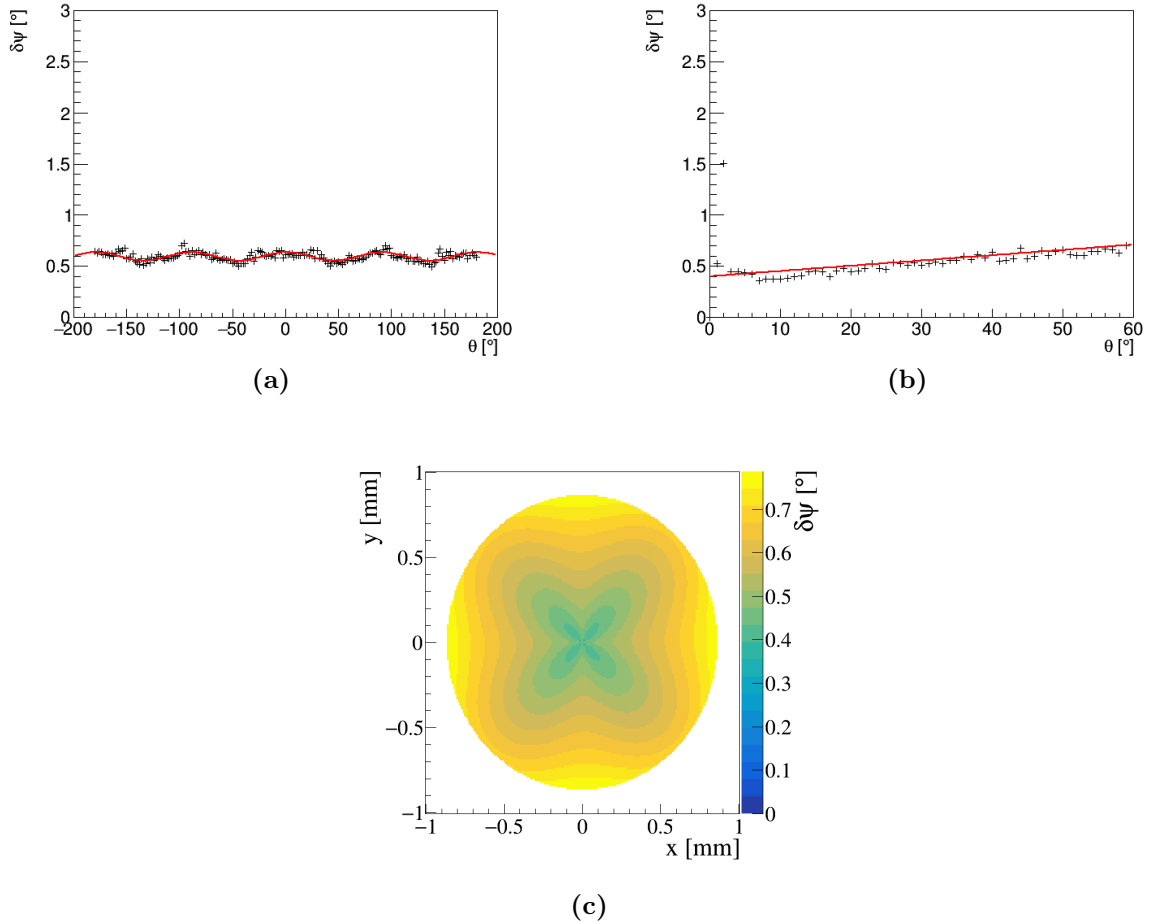


Figure 5.14: Error radius obtained by using the azimuthal and polar 1σ uncertainties (a) dependent on the original azimuthal GRB position with a fixed polar GRB position $\theta = 43.7^\circ$ and a fluence of 14.5 ph/cm^2 . (b) dependent on the original polar GRB position with a fixed azimuthal GRB position of $\phi = 33^\circ$ and a fluence of 14.5 ph/cm^2 . (c) extrapolated for the field of view of SPHiNX using (a) and (b).

The error radius was computed for the χ^2 results considering the cases of fixed θ and fixed ϕ as shown in Figure 5.14 (a) and (b). The sinusoidal dependency varying with ϕ can also be seen in the total localisation uncertainty while the dependency on θ is a linear one. In order to display the total localisation uncertainty on the whole field of view of SPHiNX, the two curves were extrapolated resulting in Figure 5.14 (c). As expected the uncertainty is higher at the edges of the SPHiNX field of view. However, the maximum is around 0.7° , representing a very satisfactory localisation result.

5.7 Conclusions and Outlook

As shown in the last section, the feasibility study investigating the SPHiNX localisation ability gives encouraging results fulfilling the criteria set for a successful polarimetric performance. Statistical uncertainties as well as systematic offsets stay inside the determined 5° limit except for some certain instances. The limiting factors for the localisation precision are the systematic offsets, which seem to be rooted in statistical fluctuations connected to the number of initial photons used for creating the required database. Nonetheless, for most cases, the obtained positions would be suitable for the purpose needed even if no other GRB mission is able to give more precise GRB locations.

In addition, first estimations including background fluctuations show promising results inside the 5° range. Further studies would be necessary as soon as the orbit of the future mission is known. Background fluctuations were considered for all three methods in the theory section for this purpose.

The possibility of a rough energy spectrum reconstruction with an energy resolution of 5 keV is a vital assumption made during the studies but introduces additional errors in the localisation methods. Nonetheless, it had to be made since a strong dependency in the polar offsets on the database energy spectrum has been observed. Further studies could be done on how these dependencies can be understood by looking at the different spectral parameters and their influences.

Another open topic is the only shortly investigated possibility of combining the different methods, for example, including the easily obtainable modulation curve results in the database methods with the purpose of improving the computation times.

More sophisticated methods, for example, machine learning algorithms in the form of neural networks or methods based on Bayesian statistics, for instance, the BALROG [31] algorithm are partly already under evaluation or planned to be. The capability of these methods of simultaneously treating spectral parameters as well as localisation parameters, or maybe even polarisation properties, would be a significant advantage. However, the systematic offsets are expected to occur in a similar order of magnitude as for the simpler methods.

In conclusion, further investigations seem to be needed in order to completely understand the entanglement of GRB location, spectrum and polarisation. Which method will be chosen for the mission depends on different parameters and the future design limitation as discussed in Section 5.4. Nonetheless, the methods used in this feasibility study already give quite satisfactory results and support the claim that SPHiNX is capable of localising GRBs precise enough for pursuing the polarisation studies planned.

Acknowledgments

To begin with, special thanks to my supervisors in Stockholm Mark Pearce and Nirmal Kumar Iyer.

Mark, thanks for letting me be part of your team for a second time and showing me how a nice research atmosphere should look like even if not all works out from time to time. Also for constantly giving advice and making me feel like my work was a vital part.

Nirmal, thanks for being the best supervisor I could imagine. I admire your knowledge and ability in keeping track of the simulations and what is going on in the lab. Thanks for working together with me in designing the methods and interpreting the results. And of course, finding my errors and helping me understand what I am actually doing. And thanks to Rakhee and you for giving me an insight into your fantastic culture.

Additional thanks to Manfred Jeitler, my Austrian supervisor, who agreed to supervise my thesis even though it is not connected to his current research field. Thanks for the talks showing inspirational curiosity and openness towards so many interesting topics and for accepting me as a master student.

Thanks to my family and friends for always supporting me without understanding what I do or why I again have to go abroad. And to my dad, for being so interested in what I do and supporting my curiosity. Please stick with watching astrophysics for sleepless people in the middle of the night, I would miss coming home to random physics questions I have no clue about.

And now to the other people in Stockholm who made my time there unforgettable.

Fei Xie, I do not even know where to start. Of course thanks for the code, the advice and the criticism but also far more. Thanks for showing me to notice shy people since there might be a wonderful person hiding behind it. For being so open-minded, talkative and inspiring. Victor Mikhalev and Mózsi Kiss, thanks for all of the useful critic, questions, talks, coding advice and tips.

Also thanks to Fran, Dennis, Mette, Zeynep and all of the rest of the astroparticle group for making me feel welcome and belonging. For making the lunch breaks and fikas so entertaining and relaxing. Especially Linda Eliasson, thanks for your inspiring curiosity, your permanent support and for being so amazing. I already miss all of the never ending chats with you.

Thanks to Moritz, for hot chocolate on late night Friday shifts and random brown bear paper discussions.

Also special thanks to my housemates in the wonderful neighbourhood of Skärholmen, who made Stockholm feel like a home and our house like a family. For listening to my complaints, distracting me on my free days and not unplugging my laptop when I left it in the kitchen overnight.

And thanks to everyone who took the time for reading and correcting my report.

List of Figures

2.1	Photon interaction with matter	5
2.2	Cross section photon interaction with matter	6
2.3	Compton scattering process	6
2.4	Pair production process	7
2.5	Generalised modulation curve	8
2.6	Duration GRBs	9
2.7	Example pectral fit using the Band function	10
2.8	Fireball model	10
2.9	Polarisation degree Compton scattering	12
3.1	InnoSat platform including SPHiNX detector	13
3.2	GRB emission model speparation by polarisation measuremts	16
3.3	SPHiNX scintillator array	17
3.4	SPHiNX detector unit	17
3.5	CAD model showing the SPHiNX detector with different shields	18
4.1	MDP uncertainty increase dependent on localisation uncertainty	20
4.2	Schematic view of the used coordinate system	21
4.3	Database grid	22
4.4	Example of a single hit pattern in the SPHiNX detector after selection	24
4.5	Spectra and maximum offset comparison for two different database spectra using χ^2 minimisation	25
4.6	Schematic view of the azimuthal detector position	26
4.7	Single hit pattern with different shields around the detector	27
4.8	Moulation curve fits for different shield	28
4.9	Obtained angles over original azimuthal angles using the modulation curve method	28
4.10	Polar angle reconstruction using the modulation curve method	29
4.11	Example of a 2D χ^2 distribution	30
4.12	Example of a Contour plot using the χ^2 method for a weak GRB	31
4.13	1D polynomial fits χ^2 distribution	31
4.14	1D polynomial fits χ^2 distribution including the modulation curve results	32
4.15	1D maximum likelihood distributions	33
5.1	Modulation curve results - Uncertainty on ϕ	36
5.2	Modulation curve results - Offsets in ϕ	37
5.3	Modulation curve results - Uncertainties on θ	38
5.4	χ^2 minimisation results - Uncertainty on ϕ	39

5.5	χ^2 minimisation results - Offsets in ϕ	40
5.6	χ^2 minimisation results - Uncertainty on θ	41
5.7	χ^2 minimisation results - Offsets in θ	42
5.8	Maximum likelihood results - Uncertainty on ϕ	43
5.9	Maximum likelihood results - Offsets in ϕ	44
5.10	Maximum likelihood results - Uncertainty on θ	45
5.11	Maximum likelihood results - Offsets in θ	46
5.12	χ^2 minimisation results - Dependency on background fluctuations of the uncertainty on ϕ	48
5.13	χ^2 minimisation results - Dependency on background fluctuations of the uncertainty on θ	49
5.14	χ^2 minimisation results - Error radius	50

List of Tables

4.1	Hit and trigger thresholds for the localisation single hit selection	23
4.2	Relevant GRBs and their properties	25

References

- [1] D. Perkins, *Particle Astrophysics*. Oxford University Press, 2nd ed., 2009.
- [2] B. P. Abbott et al., “Gravitational Waves and Gamma-Rays from a Binary Neutron Star Merger: GW170817 and GRB 170817A,” *The Astrophysical Journal Letters*, vol. 848, ID L13, 2017.
- [3] <https://www.nuclear-power.net/nuclear-power/reactor-physics/interaction-radiation-matter/interaction-gamma-radiation-matter/>. [accessed 09.04.2018].
- [4] H. Kolanoski, N. Wermes, *Teilchendetektoren*. Springer-Verlag, 1st ed., 2016.
- [5] F. Lei et al., “Compton Polarimetry in Gamma-Ray Astronomy,” *Space Science Reviews*, vol. 82, pp. 309–388, 1997.
- [6] W. Demtröder, *Experimentalphysik 2*. Springer-Verlag, 2nd ed., 2006.
- [7] M. Chauvin et al., “Preflight performance studies of the PoGOLite hard X-ray polarimeter,” *Astroparticle Physics*, vol. 72, pp. 1–10, 2016.
- [8] <https://gamma-ray.nsstc.nasa.gov/batse/grb/duration/>. [accessed 06.04.2018].
- [9] P. Mészáros, “Gamma-Ray Bursts,” *Reports on Progress in Physics*, vol. 69, pp. 2259–2321, 2006.
- [10] D. Band et al., “BATSE observations of gamma-ray burst spectra. I - Spectral diversity,” *Astrophysical Journal*, vol. 413, pp. 281–292, 1993.
- [11] T. Piran, “Gamma-ray bursts and the fireball model,” *Physics Reports*, vol. 314, pp. 575–667, 1999.
- [12] G. Ghisellini, “Gamma ray bursts: some facts and ideas,” *Astroparticle Physics*, 2001, arXiv:astro-ph/0111584.
- [13] A. Pe’er et al., “Photospheric Emission in Gamma-Ray Bursts,” *International Journal of Modern Physics D*, vol. 26, ID 1730018-296, 2017.
- [14] C. Lundman et al., “Polarization properties of photospheric emission from relativistic, collimated outflows,” *Monthly Notices of the Royal Astronomical Society*, vol. 440, pp. 3292–3308, 2014.

- [15] M. Pearce et al., “Science prospects for SPHiNX - a small satellite GRB polarimetry mission,” Accepted for publication in *Astroparticle Physics* 2018, arXiv:1808.05384.
- [16] D. Yonetoku et al., “Detection of gamma-ray polarization in prompt emission of GRB 100826A,” *The Astrophysical Journal Letters*, vol. 743, ID L30, 2011.
- [17] D. Yonetoku et al., “Magnetic Structures in Gamma-Ray Burst Jets Probed by Gamma-Ray Polarization,” *The Astrophysical Journal Letters*, vol. 758, ID L1, 2012.
- [18] Tanmoy Chattopadhyay et al., “Prompt emission polarimetry of Gamma Ray Bursts with ASTROSAT CZT-Imager,” Submitted to *The Astrophysical Journal Letters* 2017, arXiv:1707.06595.
- [19] N. Produit, “Design and construction of the POLAR detector,” *Nuclear Instruments and Methods in Physics Research A*, vol. 877, pp. 259–268, 2018.
- [20] M. L. McConnell, “High energy polarimetry of prompt GRB emission,” *New Astronomy Reviews*, vol. 76, pp. 1–21, 2017.
- [21] Internal documentation inside the SPHiNX collaboration.
- [22] L. Heckmann et al., “Gamma-ray burst localisation strategies for the SPHiNX hard X-ray polarimeter,” Submitted to the *Journal of Astronomical Telescopes, Instruments, and Systems* 2018.
- [23] J. Allison, “Recent developments in GEANT4,” *Nuclear Instruments and Methods in Physics Research A*, vol. 835, pp. 186–225, 2016.
- [24] F. Xie et al., “A Study of Background Conditions for Sphinx—The Satellite-Borne Gamma-Ray Burst Polarimeter,” *Galaxies*, vol. 6, ID 50, 2018.
- [25] <https://heasarc.gsfc.nasa.gov/W3Browse/fermi/fermigbrst.html>. [accessed 12.04.2018].
- [26] R. Brun et al., “ROOT - An Object Oriented Data Analysis Framework,” *Nuclear Instruments and Methods in Physics Research A*, vol. 389, pp. 81–86, 1997.
- [27] E. Suarez-Garcia et al., “A method to localize gamma-ray bursts using POLAR,” *Nuclear Instruments and Methods in Physics Research A*, vol. 624, pp. 624–634, 2010.
- [28] T. Hauschild et al., “Comparison of maximum likelihood estimation and chi-square statistics applied to counting experiments,” *Nuclear Instruments and Methods in Physics Research A*, vol. 457, pp. 384–401, 2001.
- [29] S. Baker et al., “Clarification of the use of CHI-square and likelihood functions in fits to histograms,” *Nuclear Instruments and Methods in Physics Research A*, vol. 221, pp. 437–442, 1987.
- [30] Internal documentation and derivations made by Nirmal Kumar Iyer.
- [31] M. J. Burgess et al., “Awakening the BALROG (BAYesian Location Reconstruction Of GRBs): A new paradigm in spectral and location analysis of gamma ray burst,” arXiv:1610.07385.